ACSNANO

www.acsnano.org

ARTICLE

Dismantling the "Red Wall" of Colloidal Perovskites: Highly Luminescent Formamidinium and Formamidinium–Cesium Lead Iodide Nanocrystals

Loredana Protesescu,[†,‡] Sergii Yakunin,[†,‡] Sudhir Kumar,[§] Janine Bär,[†] Federica Bertolotti,[⊥] Norberto Masciocchi,[⊥] Antonietta Guagliardi,[⊥,∥] Matthias Grotevent,[†,#] Ivan Shorubalko,[#] Maryna I. Bodnarchuk,[†,‡] Chih-Jen Shih,[§] and Maksym V. Kovalenko*[,†,‡]

[†]Institute of Inorganic Chemistry and [§]Institute of Chemical and Bioengineering, Department of Chemistry and Applied Bioscience, ETH Zürich, Vladimir Prelog Weg 1, CH-8093 Zürich, Switzerland

[‡]Laboratory for Thin Films and Photovoltaics and [#]Laboratory for Reliability Science and Technology, Empa–Swiss Federal Laboratories for Materials Science and Technology, Überlandstrasse 129, CH-8600 Dübendorf, Switzerland

[⊥]Dipartimento di Scienza e Alta Tecnologia and To.Sca.Lab, Università dell'Insubria, Via Valleggio 11, I-22100 Como, Italy

[∥]Istituto di Crystallografia and To.Sca.Lab, Consiglio Nazionale delle Ricerche, Valleggio 11, I-22100 Como, Italy

Supporting Information

ABSTRACT: **Colloidal nanocrystals (NCs) of $APbX_3$-type lead halide perovskites [A = Cs^+, $CH_3NH_3^+$ (methylammonium or MA^+) or $CH(NH_2)_2^+$ (formamidinium or FA^+); X = Cl^-, Br^-, I^-] have recently emerged as highly versatile photonic sources for applications ranging from simple photoluminescence down-conversion (*e.g.*, for display backlighting) to light-emitting diodes. From the perspective of spectral coverage, a formidable challenge facing the use of these materials is how to obtain stable emissions in the red and infrared spectral regions covered by the iodide-based compositions. So far, red-emissive $CsPbI_3$ NCs have been shown to suffer from a delayed phase transformation into a nonluminescent, wide-band-gap 1D polymorph, and $MAPbI_3$ exhibits very limited chemical durability. In this work, we report a facile colloidal synthesis method for obtaining $FAPbI_3$ and FA-doped $CsPbI_3$ NCs that are uniform in size (10–15 nm) and nearly cubic in shape and exhibit drastically higher robustness than their MA- or Cs-only cousins with similar sizes and morphologies. Detailed structural analysis indicated that the $FAPbI_3$ NCs had a cubic crystal structure, while the $FA_{0.1}Cs_{0.9}PbI_3$ NCs had a 3D orthorhombic structure that was isostructural to the structure of $CsPbBr_3$ NCs. Bright photoluminescence (PL) with high quantum yield (QY > 70%) spanning red (690 nm, $FA_{0.1}Cs_{0.9}PbI_3$ NCs) and near-infrared (near-IR, *ca.* 780 nm, $FAPbI_3$ NCs) regions was sustained for several months or more in both the colloidal state and in films. The peak PL wavelengths can be fine-tuned by using postsynthetic cation- and anion-exchange reactions. Amplified spontaneous emissions with low thresholds of 28 and 7.5 $\mu J\ cm^{-2}$ were obtained from the films deposited from $FA_{0.1}Cs_{0.9}PbI_3$ and $FAPbI_3$ NCs, respectively. Furthermore, light-emitting diodes with a high external quantum efficiency of 2.3% were obtained by using $FAPbI_3$ NCs.**

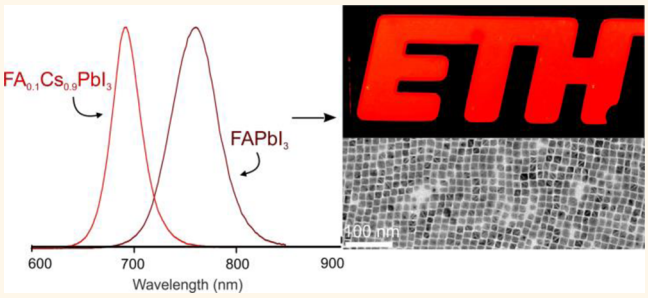

KEYWORDS: *perovskites, lead halides, nanocrystals, photoluminescence, infrared, formamidinium, cesium*

Lead halide perovskites with the generic formula of $APbX_3$ [A = $CH_3NH_3^+$ (methylammonium, MA^+), $CH(NH_2)_2^+$ (formamidinium, FA^+), or Cs^+; X = I^-, Br^-, Cl^-, or mixtures thereof] have recently been added to the pool of high-quality semiconductors (Si, GaAs, CdTe, *etc.*) after demonstrations of their highly efficient perovskite photovoltaics[1−4] with extremely high power conversion efficiencies of more than 22% (http://www.nrel.gov/ncpv/images/efficiency_chart.jpg). This outstanding performance was initially surprising because an extensive structural disorder occurs in such solution-deposited semiconductors, as exemplified by a high density of vacancies (up to 1 at. %; Schottky-

Received: January 6, 2017
Accepted: February 23, 2017
Published: February 23, 2017

DOI: 10.1021/acsnano.7b00116
ACS Nano 2017, 11, 3119–3134

type),[5] unusual ionic rotations, other structural dynamics,[5] and high ionic mobilities.[6,7] This defectiveness is fortunately counterweighted by the unusual defect-tolerant photophysics of these semiconductors, a rare situation wherein intrinsic structural defects such as vacancies, surfaces, and grain boundaries do not form or cause only a very small density of midgap states due to the peculiarities of the chemical bonding.[8−10] Many of the following physical parameters of these materials convincingly point to such a defect tolerance:[10−17] low densities of carriers (10^9−10^{11} cm^{-3}) and electronic traps (10^9−10^{10} cm^{-3}, lower than in monocrystalline Si), high carrier mobilities (2.5−1000 cm^2 V^{-1} s^{-1}), long charge carrier lifetimes (0.08−450 μs), long electron−hole diffusion lengths (2−175 μm), small carrier effective masses (0.069−0.25 m_0), high optical absorption coefficients at the absorption edge (1−4.5 × 10^4 cm^{-1}), and high photoluminescence (PL) efficiencies. These properties, which are rare in a single family of materials, enable the materials' use in a large plethora of applications beyond photovoltaics. In addition to the unusual and intrinsic defect tolerance, other important factors enable the use of these materials for a range of applications, including the facile, inexpensive, low-temperature (25−200 °C) solution-phase synthesis of these materials in all technologically relevant forms [bulk single crystals, thin films, microcrystals, or nanocrystals (NCs)]. Regarding light detection, broadband and narrowband photodetectors operating in the ultraviolet and visible near-infrared regions,[18−20] soft X-ray detectors,[21,22] or even *gamma*-detectors have been demonstrated.[23] As versatile photonic sources with emission spanning from the blue to near-infrared regions, perovskites are highly promising for use in LCD television displays and related remote phosphor applications,[24,25] light-emitting diodes,[26−33] and lasers.[34−36]

In the context of light-emission and photonic applications, colloidal perovskite NCs have emerged as materials of choice owing to the benefits of their colloidal state (solution processability, mixability with other materials, *etc.*), access to quantum-size effects, and the possibility of shape engineering, which have stimulated efforts to synthesize supported and colloidal nanostructures of hybrid and fully inorganic perovskites. For example, fully inorganic cesium lead halide NCs ($CsPbX_3$ NCs) synthesized by using simple ionic co-precipitation in nonpolar solvents have recently been shown to possess outstanding optical properties, such as broadly tunable PL (410−700 nm), a small full-width at half-maximum (fwhm = 12−40 nm for blue-to-red), and high PL quantum yields (QYs = 50−90%), providing a broad color gamut of bright emissions.[37] Considerable attention has also been devoted to hybrid perovskites ($MAPbX_3$ and $FAPbX_3$) in the form of colloidal and noncolloidal nanomaterials,[38−54] with bright PL in nearly all cases. In striking contrast with perovskites, achieving bright PL with conventional semiconductor NCs, such as CdSe, InAs, or InP, requires elaborate synthesis to ensure electronic passivation with the epitaxial layers of wider-gap semiconductors (*e.g.*, CdSe/CdS and CdSe/ZnS core−shell NCs).[55−57] Currently, colloidal $CsPbX_3$ NCs are undergoing further chemical engineering (up-scaling, shape control, further variations of the synthesis, postsynthetic reactivity)[48,58−74] and are being intensely investigated regarding their surface chemistry,[75−80] crystal structure,[81−83] single-dot emission,[84−89] and lasing[36,90] and for their use in down-conversion for displays,[91−94] active layers in light-emitting devices,[13,95−98] and solar cells.[99]

Green-emissive $CsPbBr_3$ NCs have nearly exclusively been used as an example in most of the studies mentioned above. A particularly pressing challenge is to obtain bright and stable red and near-infrared (near-IR) PL from colloidal perovskite NCs. Although $CsPbI_3$ NCs allow band-gap energies of up to 710 nm (bulk band gap) in principle, they eventually suffer from thermodynamic instability caused by the small size of the Cs^+ ion. Thus, the NCs undergo phase transitions from perovskite [*i.e.*, three-dimensional (3D) connection of PbX_6 octahedra] to a 1D wider-gap (yellow) phase with an orthorhombic lattice type. Bulk $CsPbI_3$ material is reported to form at room temperature (RT) exclusively in this yellow phase and becomes a 3D polymorph only above 315 °C.[100−103] $CsPbI_3$ NCs[37] and thin films[104,105] often initially form in a 3D phase, which is a metastable state, and a retarded phase transition still occurs within days to weeks, largely depending on the surface treatment and storage conditions, such as humidity. Our experience with $CsPb(Br/I)_3$ NCs also shows how this transformation occurs, although the transformation is much slower for higher Br contents. An alternative, phase-stable hybrid perovskite with MA^+ cations, *i.e.*, colloidal $MAPbI_3$ NCs with small sizes (10−20 nm), suffers from chemical instability due to its unavoidable conversion into PbI_2 and volatile methylamine and HI.[106,107] This challenge that is faced when attempting to obtain small and stable iodine-containing perovskite NCs and stable emissions in the red and near-IR spectral ranges is called the "perovskite red wall" in this study.

In this study, we focus on a third option for the A site cationic modulation, the use of FA^+ ions, to potentially overcome the "perovskite red wall". We have explored the two most plausible possibilities: the synthesis of $FAPbI_3$ NCs and the partial substitution of Cs^+ ions in $CsPbI_3$ with FA^+ ions. We found that both compositions resulted in highly luminescent NCs. We specifically focused on small NCs (<15 nm) to prepare highly stable and concentrated colloids when exploring the emergence and utility of quantum-size effects and directly compared our observations with those of earlier studies of cubic and nearly cubic shaped 7−15 nm $CsPbX_3$ and $MAPbI_3$ NCs.[37,49] Furthermore, when such NCs are deposited as thin, densely packed films, they may be used in optoelectronic devices, such as solar cells. For example, $CsPbI_3$ NC-based devices exhibiting power conversion efficiencies of more than 10%[83] and NCs in light-emitting diodes (LEDs) have recently been investigated.

We synthesized highly monodisperse, nearly cubic $FAPbI_3$ and $FA_{0.1}Cs_{0.9}PbI_3$ NCs with mean sizes of 10−15 nm. These NCs exhibit much higher structural stability and chemical integrity than their MA-only or Cs-only based counterparts of the same size and morphology. Detailed structural analysis has indicated (locally disordered) a 3D cubic crystal structure for $FAPbI_3$ NCs and an orthorhombically distorted 3D perovskite lattice for $FA_{0.1}Cs_{0.9}PbI_3$ NCs. The orthorhombically distorted 3D perovskite lattice is isostructural to the commonly reported orthorhombic phase of $CsPbBr_3$.[82,83] High QYs (>70%) at both red (*ca.* 690 nm, $FA_{0.1}Cs_{0.9}PbI_3$ NCs) and near-IR (*ca.* 780 nm, $FAPbI_3$ NCs) wavelengths are sustained for at least several months in a colloidal state. In addition, we show that the peak PL wavelengths can be fine-tuned by considering the postsynthetic cation- and anion-exchange reactions. When tested as optical gain media under femtosecond-pulsed excitation, $FA_{0.1}Cs_{0.9}PbI_3$ and $FAPbI_3$ NC thin films exhibited low thresholds for obtaining amplified spontaneous emissions (ASE) (28 and 7.5 μJ cm^{-2}, respectively). Owing to the

DOI: 10.1021/acsnano.7b00116
ACS Nano 2017, 11, 3119−3134

satisfactory chemical durability of these FA-based NCs, LEDs could be fabricated with a high external quantum efficiency (EQE) of up to 2.3% at near-IR wavelengths of 800 nm when using $FAPbI_3$ NCs.

RESULTS AND DISCUSSION

Phase Stability of FA-Containing Perovskite NCs. $APbX_3$ perovskites that have 3D interconnected PbX_6 are of interest for use as effective semiconductors because this configuration maximizes the electronic delocalization. These octahedra could be assembled into an ideal cubic lattice (Figure 1a, typical for bulk $FAPbBr_3$ and $FAPbI_3$ at RT) or its distorted

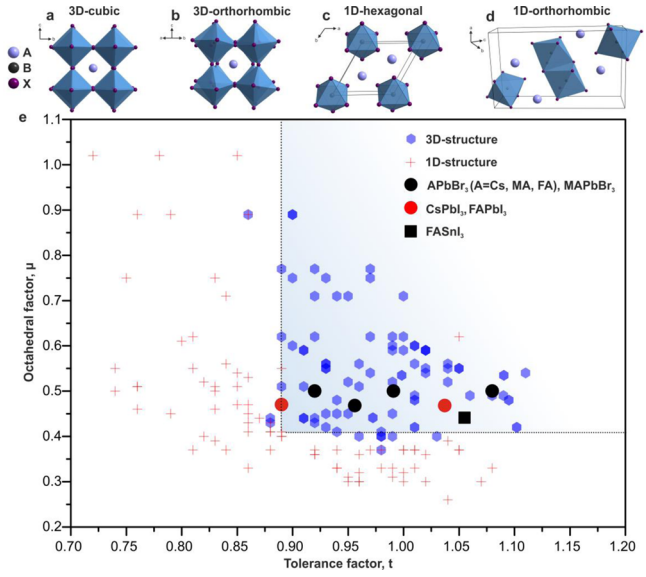

Figure 1. Survey of the reported formabilities of the 3D and 1D polymorphs of nearly all known inorganic and hybrid ABX_3 compounds, where A is an alkali metal, organic cation (MA^+ or FA^+), or other single-charged metal ion (Ag^+, Tl^+, or Cu^+); B = Pb, Sn, Mg, Ca, Sr Ba, Ti, V, Cd, Hg, Mn, Cu, Co, Zn, Tm, Dy, or Yb; and X = F, Cl, Br, of I. The tolerance and octahedral factors were mainly taken from the recent report of Travis *et al.*[114] (a) Ideal 3D cubic interconnection of PbX_6 octahedra, as observed in α-$FAPbI_3$; (b) orthorhombically distorted 3D polymorph, which is commonly reported for $CsPbBr_3$ and was observed in FA-doped $CsPbI_3$ NCs in this study; (c) 1D hexagonal lattice found in the yellow $FAPbI_3$; and (d) 1D orthorhombic lattice found in the yellow $CsPbI_3$.

versions, such as 3D orthorhombic (Figure 1b, typical for $CsPbBr_3$ at RT) or 3D tetragonal (typical for $MAPbI_3$ at RT, not shown here) versions. More details regarding the crystal chemistry of perovskites can be found in recent reviews.[108] The stabilities of these 3D polymorphs and the 3D polymorphs following their phase transformation into lower-dimensional and hence wider-band-gap structures, such as the 1D structures shown in Figure 1c,d, are of paramount importance for the practical use of perovskites in any solid-state device. In the case of iodide, severe challenges have been encountered. Bulk $CsPbI_3$ is found at RT exclusively in the yellow, orthorhombic 1D phase, which can be converted to the desired 3D polymorph (band gap at 710 nm) only above 315 °C.[100−103] Similarly, the bulk cubic 3D polymorphs of $FAPbI_3$ (so-called α-$FAPbI_3$),[12,16,102,109−111] with a band gap in the near-IR spectrum at 840 nm, are typically found in as-grown single crystals (grown above 100 °C) and exhibit thermodynamic instability toward their conversion to a wider-band-gap (yellow) hexagonal 1D phase.[12,110] The desired 3D polymorphs of $FAPbI_3$ and $CsPbI_3$ can be obtained as metastable phases in thin films, which still undergo phase transformations over several hours to several weeks and transform faster when exposed to the ambient atmosphere.[73,105,112,113]

The compositionally dependent formability of perovskites can be semiquantitatively rationalized by using geometric principles and by assuming ionic bonding. The Goldsmith tolerance factor (t) concept, which was initially proposed for metal-oxide perovskites[115] and recently extended to metal halides,[114,116−119] predicts that the radii of the constituting ions cannot deviate too far from the dense packing in an ideal cubic 3D perovskite. Correspondingly, a tolerance factor (t) can be calculated as follows:

$$t = \frac{(r_A + r_X)}{\sqrt{2}(r_B + r_X)}$$

where r_A, r_B, and r_X represent the ionic radii of each lattice site constituent. Empirical knowledge shows that stable cubic perovskites for highly ionic compounds, such as oxides and fluorides, usually fall into the range t = 0.8−1. In addition, the formability of the BX_6 octahedra is determined by the following so-called octahedral factor:

$$\mu = \frac{r_B}{r_X}$$

For μ < 0.41, a B-ion is too small and its efficient coordination will require overlapping between the X-anions; hence such a compound does not form.

Purely geometric considerations for $APbX_3$ remain highly accurate for fluorides, which are highly ionic compounds, but progressively inaccurate for heavier halides (Br, I). For the heavier halides, the difference in the electronegativity between B and X is much lower than the difference in the electronegativity between fluorides and oxides, leading to much higher covalency of the bonding. On the Pauling electronegativity scale, I is at 2.66, O is at 3.16, and F is at 3.98. Recently, Travis *et al.* indicated that the tolerance f actor calculated by using the Shannon ionic radii (which is usually used for ionic fluorides and oxides) failed to accurately predict the stability of three dozen known inorganic iodide perovskites with ABI_3 compositions.[114] These authors proposed a revised set of ionic radii for cations that is anion dependent to account for bond shortening due to increased covalency. For instance, the revised radius of Pb^{2+} was 0.98 Å in bromides and 1.03 Å in iodides, which are significantly shorter than the Shannon ion radius of 1.19 Å. For Cs^+, Br^-, and I^-, Shannon radii of 1.88, 1.96, and 2.2 Å, respectively, were used to calculate t and μ. Overall, all known stable metal bromides and iodide 3D perovskites have t>0.88 and μ > 0.41. The data from Travis *et al.*[114] for all known $APbX_3$ compounds are shown in Figure 1e, which indicates a clear-cutoff at t = 0.88 and μ = 0.41. The revised t and μ values for $CsPbBr_3$ (0.92 and 0.5) and $CsPbI_3$ (0.89 and 0.47) explain why $CsPbBr_3$ is heavily orthorhombically distorted but still 3D at RT, whereas $CsPbI_3$ is stable only at elevated temperatures. The upper boundaries for both the t and μ values are not well-defined, and stable perovskites with organic cations are found up to t = 1.1 and μ = 0.89.

Regarding hybrid $MAPbX_3$ and $FAPbI_3$ perovskites, the nonsphericity of the cation is an additional consideration. While μ-values remain unchanged, the value of t will largely depend on the estimate for the effective radius of the cation A. Travis *et*

DOI: 10.1021/acsnano.7b00116
ACS Nano 2017, 11, 3119−3134

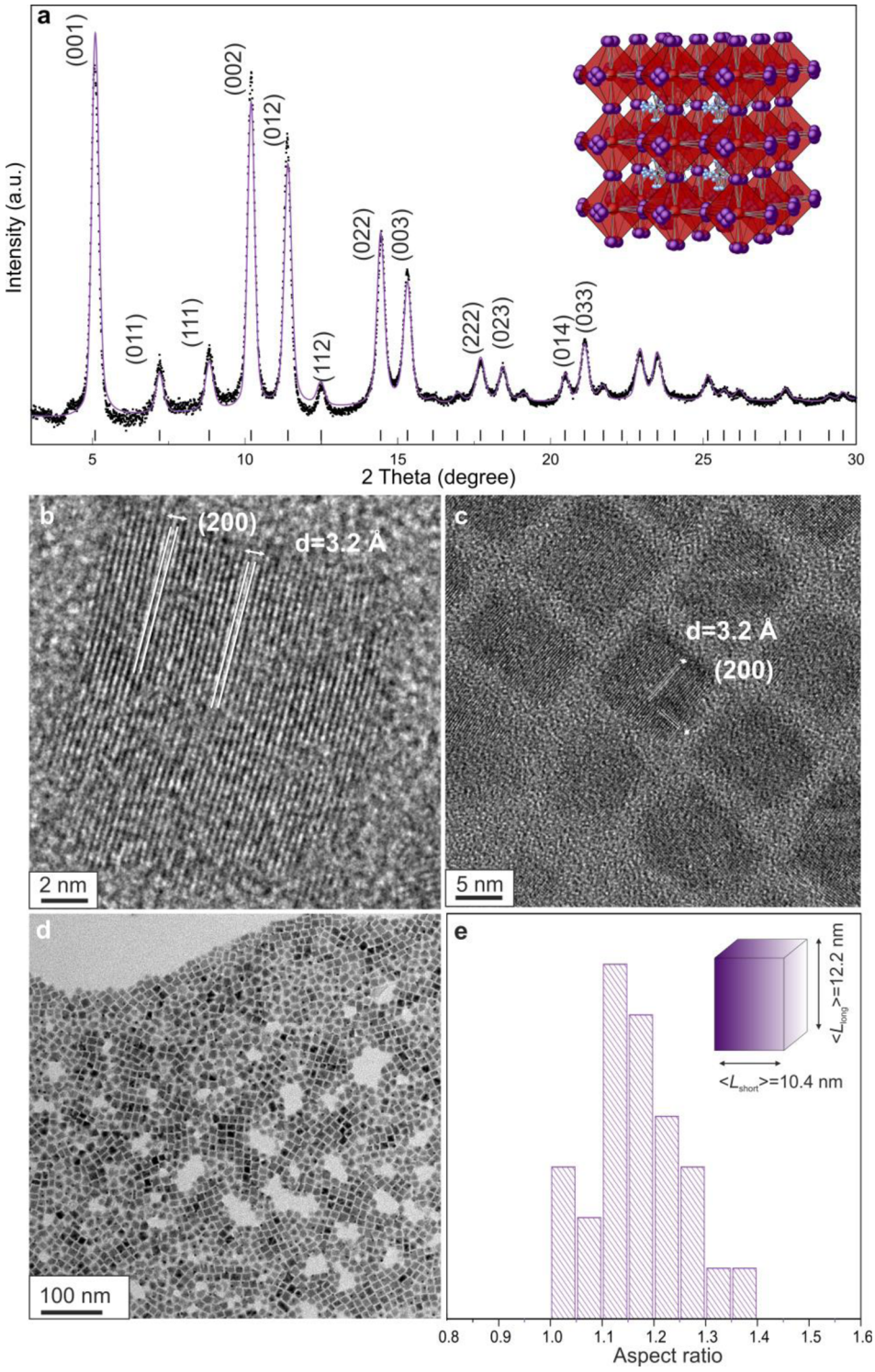

Figure 2. (a) Synchrotron XRD pattern (black) and best fit (purple, 2θ range of 3−30°; λ = 0.565 483 Å) for $FAPbI_3$ NCs using the cubic lattice, yielding a refined cell parameter of a = 6.3641 Å. The inset illustrates the cubic perovskite structure of $FAPbI_3$ and the off-axis disorder of the I^- anions. (b, c) High-resolution TEM images of $FAPbI_3$ NCs; (d) typical TEM image of $FAPbI_3$ NCs; (f) aspect ratio histogram for $FAPbI_3$ NCs.

al. estimated radii of 2.16 Å for MA^+ and 2.53 Å for FA^+ by summing the distance from the center of mass of the molecule to its furthest non-hydrogen atom and the Shannon ionic radius of the nitride (N^{3-}) anion (1.46 Å). No hybrid perovskites based on larger ions such as ethylammonium (EA^+, 2.73 Å) have been reported to date, indicating that t = 1.06 can be considered as the empirical limit ($EAPbI_3$ and $EASnI_3$ have tolerance factors of 1.07 and 1.10, respectively). The corresponding tolerance factors for known MA- and FA-based Pb and Sn perovskites are (in parentheses; along with the known stabilities of the cubic or distorted 3D lattice at RT) $MAPbI_3$ (0.95; stable),[16,110] $FAPbI_3$ (1.03, unstable),[16,110] $MASnI_3$ (0.97, stable),[120,121] $FASnI_3$ (1.06, stable),[122,123] $MAPbBr_3$ (0.95, stable),[110] $FAPbBr_3$ (1.08, stable),[94] $MAPbCl_3$

DOI: 10.1021/acsnano.7b00116
ACS Nano 2017, 11, 3119−3134

(1.00, stable),[15] and $FAPbCl_3$ (1.09, stable).[124,125] Other compounds (such as $FASnBr_3$ and $FASnCl_3$) have not been reported so far (see Table S1 for a complete survey of all compounds and Table S2 for all ionic radii considered). Clearly, no apparent explanation exists regarding the formability of 3D phases at RT for some of the compounds, based neither on t nor on μ. For instance, the 3D polymorph of $FAPbI_3$ exhibits instability despite having lower t values than the stable 3D polymorphs of $FASnI_3$ and $FAPbBr_3$. Equally puzzling is the question of why some of the other hybrid perovskites exhibit ideal cubic lattices while others are distorted at RT. Possible answers lie in recent reports highlighting the importance of vibrational entropy for stabilizing the trigonal distortion in $MAPbI_3$[126] and the entropic destabilization of α-$FAPbI_3$[127] at RT, various N−H·I hydrogen-bonding capabilities (with MA^+ being more acidic, but FA^+ having two bonding centers),[128,129] the propensity of the Pb^{2+} lone pair to express its stereochemistry,[129] and the relevance of packing density for stability (that can explain the higher stability of $FAPbBr_3$ *versus* $FAPbI_3$).[130−134]

These considerations provide guidance for creating experimental strategies to improve the stability of non-MA (*i.e.*, Cs and FA lead iodide NCs). An obvious approach, derived from the high stability of the respective Br analogues, is to prepare mixed halides with Br, such as $CsPb(Br/I)_3$, which has already been tested in several reports,[135,136] or analogous $FAPb(Br/I)_3$.[137,138] This strategy is not used here because it increases the band-gap energies and results in PL peaks below 650 nm, which are irrelevant to the perovskite "red wall" problem. To retain emissions near 700 nm and beyond, a different strategy is used, namely, partial Cs-to-FA substitution in $CsPbI_3$ NCs or partial FA-to-Cs substitution in $FAPbI_3$ NCs, to ensure that a composition-averaged t value falls within the stability window. Such cation mixing at the A site may not only optimize the structural tolerance but also cause an additional stabilizing effect from the entropy of mixing (on the order of 0.05 eV).[139] Analogous strategies have become ubiquitous in thin-film photovoltaic research. For instance, all major recent advances in the simultaneous improvement of stability and photovoltaic efficiencies have been shown with mixed-ionic compositions either on the cation side, as in $Cs_xFA_{1-x}PbI_3$ ($x \leq 0.3$) or $MA_xFA_{1-x}PbI_3$ ($x = 0.2-1$), or with simultaneous adjustment of the anionic side, such as in $Cs_{0.17}FA_{0.83}(PbI_{1-x}Br_x)_3$ ($x = 0-1$) or $(FAPbI_3)_{1-x}(MAPbBr_3)_x$ ($x = 0-0.3$) or even with a cation quadruple (Cs/MA/FA/Rb) $(PbI_{1-x}Br_x)_3$.[4,139−144] As shown below in this work, $Cs_{0.9}FA_{0.1}PbI_3$ NCs are much more stable than $CsPbI_3$ NCs.

Downsizing has a profound effect on the phase stability of inorganic NCs due to the interplay of kinetic trapping (low-T synthesis) and thermodynamics (*i.e.*, surface energy). A renowned example of this effect is the phase-pure synthesis of zinc-blende or wurzite CdSe and other II−VI compound NCs, depending on the synthesis temperature or capping ligand.[145,146] Similarly, colloidal $CsPbI_3$ NCs synthesized at 120−180 °C form in a high-temperature 3D phase. This structure remains metastable at RT and eventually converts to the 1D orthorhombic phase, and its phase stability exhibits a pronounced correlation with the processing conditions (isolation, purification, and surface treatment).[37]

However, less information is known about the phase stability of small $FAPbI_3$ NCs, which serves as one motivation for this work. Small NCs are generally known to adjust their strain distribution and lattice parameters, compared to their bulk counterparts. Detrimental effects of the bulkiness of the organic cation in α-$FAPbI_3$ NCs could be, in principle, mitigated to some extent by the slight expansion of the lattice. Recently, $FAPbI_3$ single-crystalline wires several hundred nanometers to several micrometers in diameter were reported to exhibit phase stability for up to several weeks.[147] Encouraged by the expectation that lattice adaptability will be drastically facilitated by small NCs, we synthesized ∼10 nm $FAPbI_3$ NCs and observed their full stability in a cubic α-$FAPbI_3$ polymorph without any detectable conversion upon extended storage for several months. As described in the following sections of this article, this enhanced stability may partially originate from the lattice expansion.

Synthesis and Crystal Structure of $FAPbI_3$ NCs. We developed two synthesis methods for obtaining nearly cubic 10−15 nm $FAPbI_3$ NCs (Figure 2) by using strategies from our earlier studies of $CsPbX_3$ and $FAPbBr_3$ NCs.[37,148] In the method 1 (the two-precursor approach), lead halide is reacted with FA-oleate. Briefly, PbI_2 (0.086 g, 0.187 mmol) was dissolved at 80 °C in 1-octadecene (ODE, 5 mL) containing oleic acid (OA, 1 mL) and oleylamine (0.5 mL, OLA), which resulted in a clear yellow solution. This solution was kept at 80 °C and swiftly injected with a solution of FA-oleate in ODE (0.25 M, 2 mL). Unlike the synthesis of $CsPbI_3$ NCs,[37] which required a high excess of Pb (molar ratio Pb:Cs = 3.75) and high temperatures (120−200 °C), $FAPbI_3$ NCs form exclusively under conditions with excess FA (FA:Pb = 2.7) and at 80 °C (see further details in the Methods section). In addition, excess OA is necessary, presumably to maintain the protonation of FA. When excess OLA is present, $FAPbI_3$ NCs decompose rather quickly, often before the solution can be cooled to RT and the NCs can be isolated. The solvent used for this reaction (ODE) can also be replaced with mesitylene without compromising the quality of the NCs. Attempts to replace the traditional OA/OLA ligand couple with shorter-chain molecules, such as octanoic acid and octylamine, were unsuccessful. The crude solution was centrifuged to obtain the NCs. Next, the NCs were redispersed in toluene and precipitated again using acetonitrile as a nonsolvent. This purification step was repeated two more times.

The formation of $FAPbI_3$ NCs was not observed at higher injection temperatures (>80 °C) when using this method; however, at temperatures below 50 °C, nanosheets with sizes between 0.2 and 0.5 μm were obtained (Figure 3). According to Weidman *et al.*,[149] the observed emission peak at approximately 580 nm corresponds to nanoplatelets with the chemical formula $(Oleyl\text{-}NH_3)_2[FAPbI_3]PbI_4$ and with two layers of corner-sharing PbI_6 octahedra terminated by OLA ligands.[149] Similar PL peaks or absorption edge wavelengths were previously observed for two-layer lead iodide perovskites obtained during the thickness-controlled synthesis of colloidal and supported nanostructures[42,46] and in Ruddlesden−Popper hybrid phases.[150]

In method 2 (three-precursor approach), molecular OLA was excluded. Briefly, a mixture of FA-oleate and Pb-oleate was formed by reacting FA-acetate (0.078 g, 0.75 mmol) and $Pb(acetate)_2$ (0.076 g, 0.2 mmol) with OA (dried, 2 mL) in ODE as a solvent (8 mL). This mixture was heated to 80 °C, and oleylammonium iodide (OLA:HI, 0.237 g, 0.6 mmol) dissolved in toluene (anhydrous, 2 mL) was injected at 80 °C before quenching the reaction after 1 min (see the Materials and Methods section for further details).

DOI: 10.1021/acsnano.7b00116
ACS Nano 2017, 11, 3119−3134

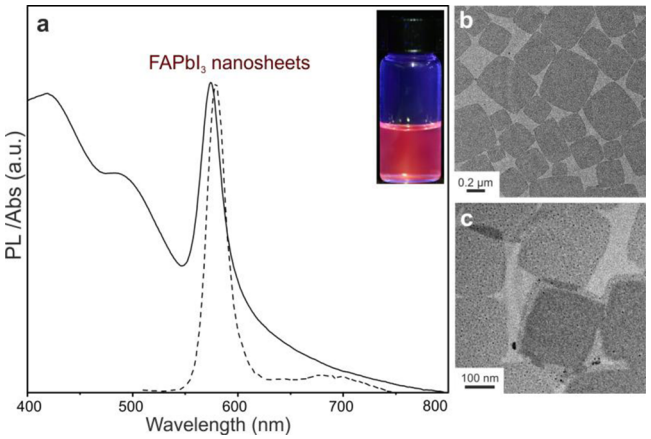

Figure 3. (a) PL and absorbance spectra for $FAPbI_3$ nanosheets. (b and c) Corresponding TEM images showing 0.1−0.6 μm nanosheets.

Both methods yield highly monodisperse $FAPbI_3$ NCs (Figure 2d) with nearly cubic shapes ($\langle L_{short} \rangle$ = 10 nm, $\langle L_{long} \rangle$ = 12 nm, Figure 2e). The high-resolution transmission electron microscopy (TEM) images show an interplanar distance of 3.2 Å associated with the (200) reflection plane.

To accurately determine the crystal structure of the $FAPbI_3$ NCs, we obtained synchrotron X-ray total scattering measurements of the NCs in a toluene solution (Figure 2a) at the X04SA-MS4 Powder Diffraction Beamline of the Swiss Light Source (Paul Scherrer Institute, Villigen, CH).[151] The XRD patterns suggested the occurrence of a cubic structure corresponding to the α-phase of the bulk material.[137] However, similar to previous observations of other lead halide perovskites (single-crystalline $CsPbCl_3$[153] and $FAPbBr_3$ NCs[148]), we modeled the splitting *off-axis* of the I^- ion position (considering the Pb−I−Pb axis). Notably, all reported structural analyses of the bulk α-$FaPbI_3$ indicate regular positioning of the I atoms along the Pb−I−Pb axis.[12,102,109,110,127,129,152] After disordering the I^- anions into four equivalent positions, conventional Rietveld refinement provided Pb−I−Pb bond angles of 166.8°, which was similar to the scenario observed in our previous study of $FAPbBr_3$ NCs.[148] This positional splitting also explains the anomalous thermal parameter of I^-, which is reported to be a severely anisotropic (disk-like) ellipsoid.[152]

Next, we modeled the X-ray diffraction (XRD) patterns of the NCs using Debye function analysis (DFA) based on the Debye scattering equation (DSE)[154,155] by combining the disordered crystal structure and the NC shape within a unifying atomistic model. To account for the slightly anisotropic NC morphology suggested by TEM analysis, a bottom-up approach was used to generate the bivariate population of NCs grown according to two independent directions, one along the *c*-axis and one parallel to the *ab*-plane (Figure S2). The small lattice expansion observed herein (0.1% with respect to the bulk value)[129] could be a manifestation of surface inflation, possibly stabilizing the NCs. Because the observed lattice parameter (6.3641 Å) is averaged over the inner (core) and outer (shell) interatomic contacts of the entire NC population and less than a quarter of atoms lie within 1 nm of the surface, the actual magnitude of the surface-relaxation effect is likely underestimated.

Synthesis and Crystal Structure of $FA_xCs_{1-x}PbI_3$ NCs ($x \leq 0.1$). First, PbI_2 (0.086 g, 0.187 mmol) was dissolved at 120 °C under vacuum in ODE (5 mL) containing OA (1 mL) and OLA (0.5 mL) to form a clear yellow solution. Next, the solution was heated to 165 °C (under N_2) and a mixture of FA-oleate (0.25 M in ODE, 0.27 mL) and Cs-oleate (0.125 M in ODE, 0.27 mL) was injected, resulting in overall molar ratios of A:Pb = 0.53:1 (A = FA+Cs) and FA:Cs = 2:1. Next, the NCs were isolated using the same procedure described above for $FAPbI_3$ NCs. Rutherford backscattering (RBS) measurements, energy-dispersive X-ray spectroscopy (EDX), and inductively coupled plasma optical emission spectrometry (ICP-OES) all indicated that the Cs:Pb atomic ratio was 0.9:1 (near the ideal ratio of 1:1 for FA-free synthesis). To accurately identify the crystal structures of the NCs, synchrotron XRD patterns were collected. A 3D perovskite orthorhombic lattice (space group: *Pbnm*) was found in both FA-doped and FA-free $CsPbI_3$ NCs that was isostructural to the lattice commonly reported for bulk and nanocrystalline $CsPbBr_3$ (Figure 1b).[14,82,83] Additional details regarding this rather surprising finding will be published elsewhere. Herein we note that the insertion of approximately 10% FA^+ cations into the $CsPbI_3$ lattice only marginally affects the cell parameters and does not change the relative intensities of the diffraction peaks because the FA^+ cations are light elements with much lower X-ray scattering power (Figure 4a). Also for these materials, the results from the DFA model show a nearly cubic shape (Figure S3), which is in good agreement with the TEM analysis (Figure 4b−e).

When the A:Pb ratio is varied from 0.53:1 to 2.7:1 and the FA:Cs ratio is varied from 0.5:1 to 6:1, the position of the PL peak for $FA_xCs_{1-x}PbI_3$ NCs is not affected considerably (<10 nm, this small shift could be induced by the NC size variation, Figure S4). Furthermore, we have attempted to use another method, namely, a reverse injection of PbI_2 precursor into a Cs-oleate and FA-oleate mixture in ODE. However, this method also lacks apparent tunability of the PL peak. These observations suggest a preference for a single FA/Cs composition. Indeed, RBS, EDX, and ICP-OES analyses all indicated a 10% deficit in Cs^+ compared to $CsPbI_3$ NCs. Finally, it is also plausible that the FA^+ cations only substitute for Cs^+ in the outermost shell of the NCs.

Optical Properties of $FAPbI_3$ NCs and $FA_{0.1}Cs_{0.9}PbI_3$ NCs. The $FAPbI_3$ NCs exhibit PL emission peaks at approximately 770−780 nm with typical QYs greater than 70% and a fwhm of 45 nm. For comparison, the PL peaks at 810−840 nm are commonly reported for bulk and thin-film α-$FAPbI_3$.[12,109,112] The insertion of FA^+ into the $CsPbI_3$ NCs structure increased the period of stability of the $CsPbI_3$ NCs from several days to a few months. The emission peak of $FA_{0.1}Cs_{0.9}PbI_3$ NCs appears at 685 nm, and the obtained QYs exceeded 70% (Figure 5a). Both $FAPbI_3$ and $FA_{0.1}Cs_{0.9}PbI_3$ NCs retain their high QY in solution (with less than 5% relative decrease) after several months of storage at ambient conditions (Figure 5a). The PL time-resolved traces of $FAPbI_3$ NCs exhibited nearly monoexponential characteristics with average relaxation times of 70 ns (Figure 5b), which were similar to the relaxation times observed for $FAPbI_3$ thin films.[138] $FA_{0.1}Cs_{0.9}PbI_3$ NCs have short radiative lifetimes of approximately 51 ns. The decay of PL in the solutions did not noticeably change with the number of washings for all of the studied samples. In contrast with the solution measurements, the radiative times in the films are faster, especially for NCs washed multiple times (down to 5 ns; Figure S5). As expected,

DOI: 10.1021/acsnano.7b00116
ACS Nano 2017, 11, 3119−3134

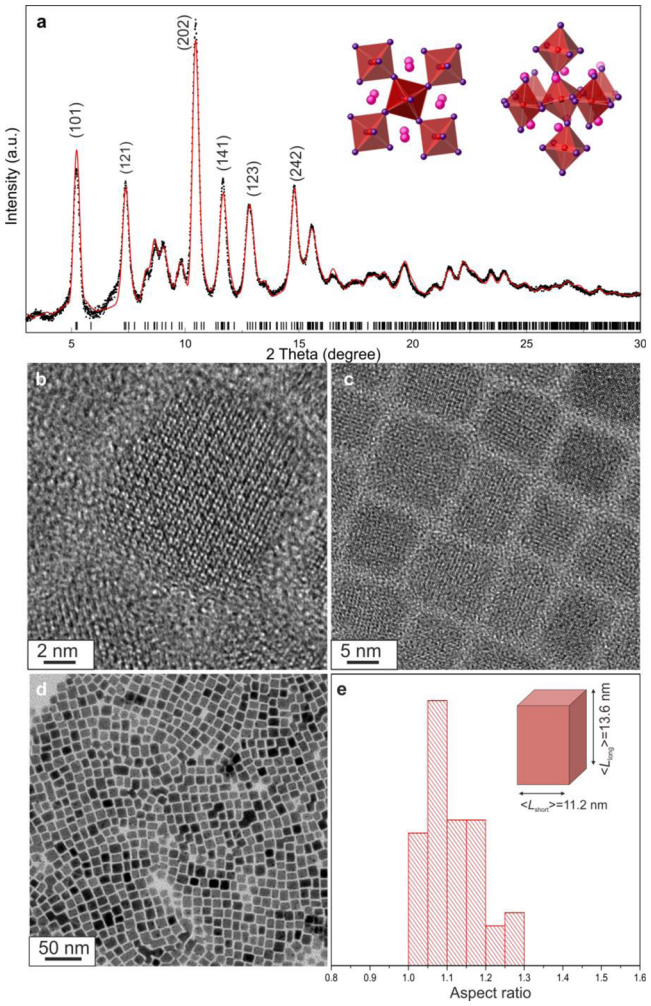

Figure 4. (a) Synchrotron XRD pattern (black) and best fit (red, 2θ range of 3−30°; λ = 0.565 483 Å) for $FA_{0.1}Cs_{0.9}PbI_3$ NCs using the γ-orthorhombic phase of $CsPbI_3$. The inset illustrates the γ-orthorhombic phase of $CsPbI_3$. (b, c) HRTEM and (d) TEM images for $FA_{0.1}Cs_{0.9}PbI_3$ NCs, along with (e) a histogram of the aspect ratio.

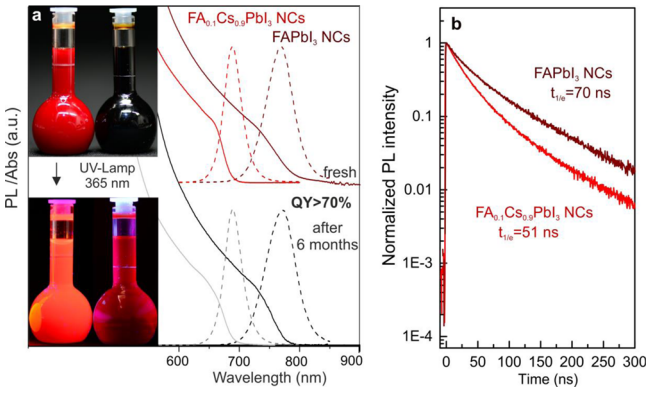

Figure 5. (a) Optical absorption and PL spectra of $FAPbI_3$ NCs and $FA_{0.1}Cs_{0.9}PbI_3$ NCs before and after 6 months of storage. The insets contain photographs of the $FAPbI_3$ NCs and $FA_{0.1}Cs_{0.9}PbI_3$ NCs colloidal solutions in toluene under daylight (upper image) and under a UV lamp (λ = 365 nm; lower image). (b) PL decay traces for colloidal $FAPbI_3$ and $FA_{0.1}Cs_{0.9}PbI_3$ NCs.

this effect is accompanied by decreasing QYs (Figure S6). The $FAPbI_3$ NC films exhibited better QY retention under identical testing/processing conditions (Figure S6). Particularly, when washed and annealed at 100 °C (1 h), the $FAPbI_3$ NC films retained a QY of 20%. Analogous tests with $FA_{0.1}Cs_{0.9}PbI_3$ NCs resulted in QYs < 10%. Both $FA_{0.1}Cs_{0.9}PbI_3$ and $FAPbI_3$ NCs exhibit much better chemical durability than their $CsPbI_3$ and $MAPbI_3$ cousins of similar size and shape (see comparison with our earlier work[37,49] in Table S3).

Cation/Anion Exchange. Although fast anion exchange is well-documented and commonly used for fine-tuning the wavelengths of PL peaks,[64,65] cation exchange has been reported only in thin films where FA^+ is replaced by MA^+ or *vice versa* and the underlying crystal structure is retained.[156−158] Herein, we show that Cs^+ and FA^+ can be exchanged by using FA-oleate or Cs-oleate as precursors (Figure 6a), despite the

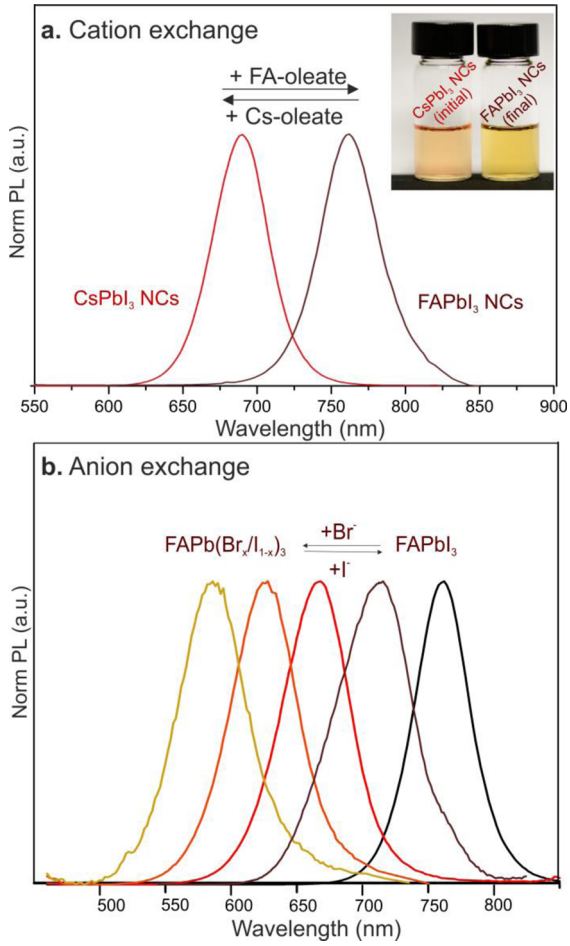

Figure 6. (a) PL spectra before and after cation exchange within $FAPbI_3$ NCs (or $CsPbI_3$ NCs) using Cs-oleate (or FA-oleate). (b) PL spectra before and after anion exchange of $FAPbI_3$ NCs using OAm^+Br^- (or OAm^+I^-) showing the possibility of tuning the band gap from 570 to 780 nm.

costs associated with the atomic rearrangement between cubic $FAPbI_3$ and γ-orthorhombic $CsPbI_3$. Furthermore, $FAPbI_3$ NCs can be subjected to anion exchange, resulting in band gaps of 570 to 780 nm (Figure 6b). The halide sources for anion exchange were oleylammonium halides (OAm^+I^- and OAm^+Br^-; see the Materials and Methods section for further details). After partial exchange of I^- with Br^- within $FAPbI_3$

DOI: 10.1021/acsnano.7b00116
ACS Nano 2017, 11, 3119−3134

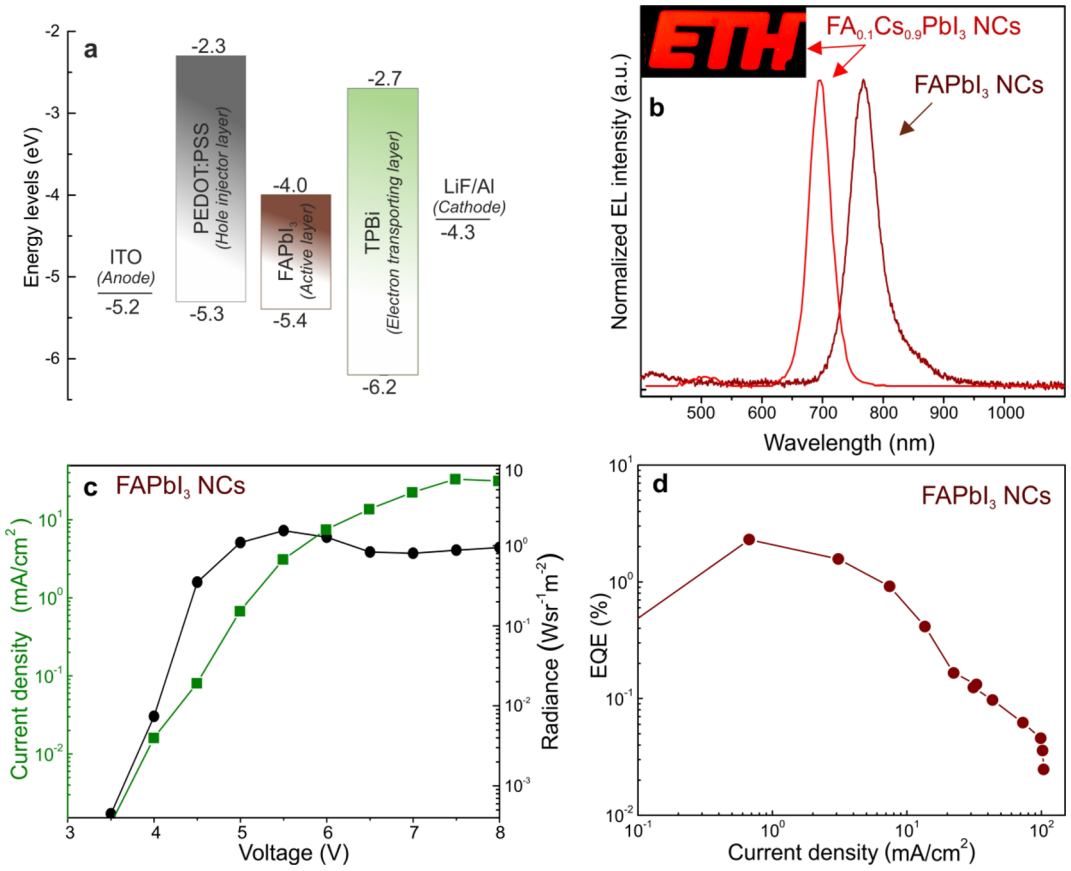

Figure 7. (a) Schematic energy diagram of LED devices; the values for the energy levels for $FAPbI_3$ correspond to those reported in the literature for thin films.[161] (b) EL spectra for $FaPbI_3$ NCs and $FA_{0.1}Cs_{0.9}PbI_3$ NCs. Inset: Photograph of LED using $FA_{0.1}Cs_{0.9}PbI_3$ NCs as the active layer. The use of the ETH logo as a pattern in the LED active layer is done with permission from ETH Zürich. (c) Current density *versus* voltage (J–V) and radiance *versus* voltage characteristics shown for $FAPbI_3$ NC-based devices, and the highest external quantum efficiency *versus* current density characteristics shown for the $FAPbI_3$ NC-based devices.

NCs, QYs are maintained at high values and the fwhm are preserved for PL peak maxima above 670 nm. Further incorporation of Br ions decreases the QY, culminating in a low value of only a few percent for (nearly) pure $FAPbBr_3$ NCs.

Light-Emitting Diodes. High PL QYs and the thermodynamic stability of colloidal $FAPbI_3$ and $FA_{0.1}Cs_{0.9}PbI_3$ NCs motivated us to investigate their potential use in electroluminescent devices. As illustrated in Figure 7a (additional details are provided in the Materials and Methods section), LEDs were fabricated by sequentially spin coating a 35 nm hole-transporting layer of PEDOT:PSS and an ~30 nm emissive layer of colloidal $FAPbI_3$ (or $FA_{0.1}Cs_{0.9}PbI_3$) NCs. Subsequently, a 35 nm layer of TPBi, an electron-transporting layer (ETL), was thermally evaporated under vacuum (1×10^{-7} mbar). Finally, a 1 nm electron injection layer of LiF and a 100 nm Al cathode layer were deposited using a patterned shadow mask. All devices were tested under ambient conditions. As shown in Figure 7b, a near-IR electroluminescence (EL) emission peak was observed at 772 nm when using $FAPbI_3$ NCs, which was consistent with the PL emission peak. The current density *versus* voltage (J–V) and radiance *versus* voltage characteristics are shown in Figure 7c. A radiance of 1.54 W sr^{-1} m^{-2} was realized at a driving voltage of 5.5 V. A relatively low radiance resulted from the reduced carrier transport in the electron/hole transport layers,[159] which is a problem that could be mitigated in the future by engineering the surfaces of the NCs. Suboptimal charge transport was also reflected at the high turn-on voltages of the devices (≥4.0 V). An EQE of 2.3% at a current density of 0.67 mA cm^{-2} was determined for LEDs comprising $FAPbI_3$ NCs (Figure 7d). Notably, such an EQE represents the highest value among all perovskite NC-based perovskite LEDs demonstrated in the near-IR range (>750 nm). The highest recently reported EQE values for perovskite NC-based devices in the red region are 6.3% for $CsPb(Br/I)_3$ NCs (650 nm)[30] and 5.7% for $CsPbI_3$ NCs (698 nm).[97] When using $FA_{0.1}Cs_{0.9}PbI_3$ NCs as an active layer, a similar device architecture yielded an EL peak at 692 nm (Figure 7b). The photograph of the corresponding large-area (~1.5 cm^2) deep-red LED device is presented in the inset of Figure 7b. The resulting device exhibited the highest EQE of 0.12% and a maximum luminance of 4.3 cd/m^2 (Figure S7). Although these results are preliminary, we believe that further optimizations, such as the introduction of metal-oxide carrier transporting layers[27,160] in the device architecture, along with NC surface engineering would eventually lead to higher EQE values.

Amplified Spontaneous Emissions. Lead halide perovskites have been intensely investigated regarding their ability to act as optical gain materials, particularly as thin films,[34,162,163] NCs,[36,49,164] and nanowires.[35,147,165] Most reports point to rather low lasing thresholds, particularly when comparing colloidal quantum dots or organic emitters. Due to thermodynamic instability of $CsPbI_3$, a particularly persistent challenge for small iodide-based $CsPbX_3$ NCs (X = Br/I, I) is how to obtain ASEs in the red region,[36] which is discussed in

DOI: 10.1021/acsnano.7b00116
ACS Nano 2017, 11, 3119–3134

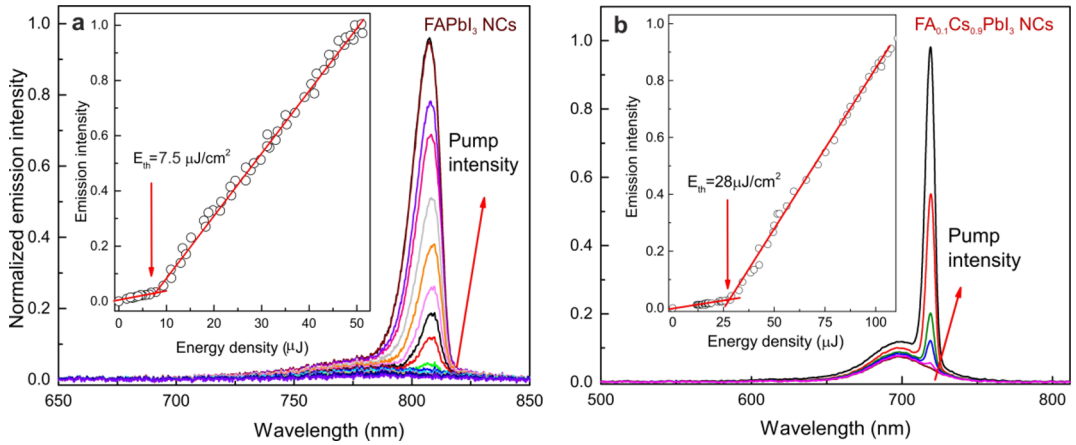

Figure 8. Amplified spontaneous emissions for films prepared from (a) $FAPbI_3$ NCs using dip-coating with heat treatment at 90 °C and (b) $FA_{0.1}Cs_{0.9}PbI_3$ NCs using simple drop-casting and heat treatment at 50 °C.

detail in the introduction section. The ASE thresholds for $CsPbBr_{3-x}I_x$ increase while the ratio of I^-/Br^- (*i.e.*, with red shift) increases under the same testing conditions used in our laboratory, and no ASE could be obtained beyond 630 nm (at RT). Having robust infrared NC emitters with low-threshold ASEs would be highly advantageous because colloidal NCs could be uniformly coated on nearly any substrate for engineering resonators and various lasing modes. The increased stabilities of $FAPbI_3$ and $FA_{0.1}Cs_{0.9}PbI_3$ NCs allow us to observe ASEs at RT in compact NC films (100 fs pulsed excitation) deposited on glass substrates (Figure 8). ASEs appear as a narrow band (fwhm of 10−12 nm) red-shifted with respect to the PL maxima (by 30 and 50 nm for $FA_{0.1}Cs_{0.9}PbI_3$ and $FAPbI_3$, respectively). Films of $FA_{0.1}Cs_{0.9}PbI_3$ NCs dried at 50 °C exhibited ASE thresholds at approximately 28 $\mu J\ cm^{-2}$. For the drop-casted films, the ASE thresholds decreased under the processing conditions that favored sintering of the perovskite NCs (partial ligand desorption by repetitive washing steps and/or annealing of the films at 90 °C). For instance, when the $FAPbI_3$ films were annealed at 100 °C, their ASE thresholds decreased from 0.5 mJ cm^{-2} to 24 $\mu J\ cm^{-2}$. Even lower ASE thresholds were obtained for 100 nm compact films with smooth mirror-like surfaces that were obtained by repetitive dip-coating (with 90 °C annealing after each dip). The resulting ASE threshold of 7.5 $\mu J\ cm^{-2}$ was among the lowest values of the red-to-near-IR emitting perovskites (5−10 $\mu J\ cm^{-2}$).[36,147,166−169]

Conclusions. In summary, we synthesized $FAPbI_3$ and $FA_{0.1}Cs_{0.9}PbI_3$ NCs that exhibit stable and highly efficient near-IR (780 nm) and red emissions (680 nm), respectively. Simple ligand-assisted synthesis procedures were used that yielded stable colloids with consistent sizes (10−15 nm) and near-cubic shapes. Using synchrotron X-ray scattering, we observed a locally disordered cubic lattice for $FAPbI_3$ NCs and a γ-orthorhombic structure for $FA_{0.1}Cs_{0.9}PbI_3$ NCs. Satisfactory chemical durability of these NCs was illustrated by the retention of high QYs (>70%) for months by the successful fabrication of LEDs, with EQEs reaching 2.3%, and by the low-threshold lasing from the compact films of these NCs. Future studies of these NCs should focus on their compositional engineering (*i.e.*, the formation of $Cs_{1-x}FA_xPbBr_yI_{3-y}$) and the optimization of LED devices. Applications in photovoltaics can be envisaged, wherein such NC colloids can be employed as inks for deposition of absorbing layers. In this context, and in contrast with conventional molecular solutions used as inks, remarkable possibilities can be conceived from facile compositional engineering, ligand removal combined with low-temperature sintering for recrystallization, or other methods of surface coating for maintaining quantum-size effects.

MATERIALS AND METHODS

Synthesis of the Formamidinium Oleate (FA-Oleate) Precursor Solution (~0.25 M of FA^+). Formamidinium acetate (FA-acetate, 0.521 g, 5 mmol, Aldrich, 99%), ODE (16 mL, Aldrich, 90%, vacuum-dried at 120 °C), and OA (11.3 mmol, 4 mL, Aldrich, 90%) were added to a 50 mL round-bottom flask. The mixture was degassed for 10 min at RT and then heated under nitrogen to 130 °C, which yielded a clear solution. This solution was dried for 30 min at 50 °C under vacuum. FA-oleate needs to be heated to 100 °C under nitrogen before use because it often precipitates when stored at cold RT.

Synthesis of the Cesium-Oleate Precursor (~0.06 M of Cs^+). Cs_2CO_3 (0.433 g, 1.33 mmol, Aldrich, 99%), ODE (20 mL), and OA (1.25 mL, 3.53 mmol) were mixed in a 50 mL round-bottom flask, dried for 1 h at 120 °C, and heated to 150 °C until the solution became clear. Cs-oleate was heated to 100 °C before use because it often precipitates when cooled to RT.

Preparation of Oleylammonium Halide (OAmX, X = Br, I). Ethanol (100 mL, Aldrich, absolute, > 99.8%) and OLA (12.5 mL, Acros Organics, 80−90%) were combined in a 250 mL two-neck flask and vigorously stirred. The reaction mixture was cooled in an ice−water bath before adding HBr (8.56 mL, 8% aqueous solution, Aldrich) or HI (10 mL, 57% aqueous solution, Aldrich, without stabilizer) dropwise to yield a final OLA:HX molar ratio of 1:2. The mixture was left to react overnight under flowing N_2. Next, the solution was dried under vacuum, and the obtained product was recrystallized multiple times from diethyl ether and then isolated as a white powder by vacuum-drying at 80 °C.

Synthesis of $FAPbI_3$ NCs *via* the Two-Precursor Method (Method 1). PbI_2 (0.086 g, 0.187 mmol, Aldrich, 99%) and ODE (5 mL) were added to a 25 mL round-bottom flask, dried for 1 h at 120 °C, and mixed with OA (1 mL, vacuum-dried at 120 °C) and OLA (0.5 mL, vacuum-dried at 120 °C). When the PbI_2 was fully dissolved and the mixture was cooled to 80 °C, the preheated FA-oleate precursor (2 mL, yielding a molar ratio FA:Pb = 2.7) was injected. After 10−60 s of stirring, the solution was cooled to RT in a water bath. The crude solution was centrifuged for 5 min at 12 100 rpm, the supernatant solution was discarded, and the precipitate was redispersed in toluene. Next, NCs were subjected to two cycles of precipitation and redispersion by adding acetonitrile (volume ratio of toluene:acetonitrile = 3:1) to destabilize the colloids, followed by centrifuging and dispersing the NCs in toluene again. In an alternative

DOI: 10.1021/acsnano.7b00116
ACS Nano 2017, 11, 3119−3134

purification procedure, the supernatant solution was discarded after centrifuging the crude solution for 5 min at 12 100 rpm, and the precipitate was dispersed in 400 μL of hexane and centrifuged again. The precipitate was suspended in 6 mL of toluene and centrifuged at 4400 rpm for 3 min. Next, the precipitate was discarded and the supernatant solution was used for further experiments.

Synthesis of $FAPbI_3$ NCs *via* the Three-Precursor Method (Method 2). $Pb(acetate)_2{\cdot}3H_2O$ (0.076 g, 0.2 mmol, Aldrich, 99.99%), FA-acetate (0.078 g, 0.75 mmol), ODE (8 mL, dried), and OA (2 mL, dried) were combined in a 25 mL three-neck flask and dried under vacuum for 30 min at 50 °C. The mixture was heated to 80 °C under N_2, followed by the injection of OAmI (0.237 g, 0.6 mmol in 2 mL of toluene). After 10 s, the reaction mixture was cooled in the water bath. The crude solution was centrifuged for 5 min at 12 100 rpm, the supernatant was discarded, and the precipitate was redispersed in toluene and washed two times with acetonitrile (3:1 toluene/acetonitrile).

Synthesis of FA-Doped $CsPbI_3$ NCs. PbI_2 (0.086 g, 0.187 mmol) and ODE (5 mL) were added to a 25 mL round-bottom flask. The resulting suspension was dried for 1 h at 120 °C. Under nitrogen, OA (1 mL, dried) and 0.5 mL of predried OLA were added. When the PbI_2 dissolved, the mixture was heated to 165 °C. A preheated precursor solution consisting of FA-oleate (0.27 mL) and Cs-oleate (0.27 mL) was injected and then cooled to RT in a water bath after 1 min of stirring. NCs were isolated and purified as described for $FAPbI_3$ NCs.

Anion Exchange. Anion-exchange reactions were performed in 1 mL of toluene and OAmBr (concentrations from 1 to 10 mg/mL) by adding 200 μL of the $FAPbI_3$ NCs (10 mg/mL) and then stirring the mixture for 10 min at RT. The NCs were isolated by adding 0.4 mL of acetonitrile followed by centrifugation and redispersion in toluene.

Cation Exchange. The cation-exchange reactions were performed in 1 mL of toluene solution containing Cs-oleate or FA-oleate, which were prepared by diluting 50−500 μL of the Cs-oleate or FA-oleate precursors as described above with toluene. $FAPbI_3$ NCs (10 mg/mL) or $CsPbI_3$ NCs were added, and the mixture was stirred for 10 min at RT. The NCs were isolated by adding 0.4 mL of acetonitrile followed by centrifugation and redispersion in toluene.

Preparation of Films by Dip-Coating. Next, 200 μL of acetonitrile was added to 1 mL of the as-synthesized $FAPbI_3$ NCs dispersion and centrifuged for 3 min. Then, the precipitate was dispersed in 1 mL of toluene. This purification process was repeated three more times. The final dispersion solution was passed through a 0.45 μm PTFE filter, and an additional 2 mL of toluene was added to give an approximate NC concentration of 1 mg/mL. Thin films were prepared on acetone-cleaned glass slides by withdrawing the slide from the dispersed and washed $FAPbI_3$ NCs at a rate of 10 mm min^{-1} and then baking the slide at 90 °C for 10 min. Next, the slide was cooled to RT and immersed in pure toluene before slowly withdrawing it again (10 mm min^{-1}) and drying it at 90 °C for 1 min. This sequence was repeated 10 times to yield a film with a thickness of approximately 100 nm. The thickness of the film was measured using a Dektak XT Bruker with Bruker Vision 64, version 5.51 software.

Fabrication of LED Devices. Indium tin oxide (ITO)-coated glass substrates with a sheet resistance of 15 Ω/□ were purchased from Lumtech Corp. The hole injection material poly(3,4-ethylenedioxythiophene)-poly(styrenesulfonate) (PEDOT:PSS) was purchased from Heraeus (Clevios P VPCH 8000). The electron transport material 2,2′,2″-(1,3,5-benzenetriyl)tris(1-phenyl-1*H*-benzimidazole) (TPBi) was supplied by e-Ray Optoelectronic. The electron injection material lithium fluoride (LiF) was purchased from Acros Organics, and aluminum (Al) pellets were purchased from Kurt J. Lesker Co. Ltd. All the materials were used without any further purification.

First, patterned ITO-coated glass substrates were rinsed with a mixture of Extran MA02 neutral detergent and deionized (DI) water (1:3). Subsequently, substrates were sonicated in DI water, acetone, and 2-propanol for 10 min each. Then, the substrates were treated in an oxygen plasma for 10 min. The aqueous solution of PEDOT:PSS was spin-coated on the precleaned ITO glass at a speed of 4000 rpm for 20 s and then annealed at 120 °C for 30 min under ambient conditions. All of the annealed substrates were transferred into a nitrogen-filled glovebox for the deposition of subsequent layers. The colloidal suspension of $FAPbI_3$ NCs in toluene (10 mg/mL) was spin-coated at 2500 rpm for 20 s. Then, the ETL was deposited by the thermal evaporation of TPBi in a vacuum chamber at $\sim 1 \times 10^{-7}$ mbar. Finally, a 1 nm LiF electron injection layer and a 100 nm Al cathode layer were deposited through the shadow mask. Each substrate is patterned to realize four devices, each with an active area of 15 mm^2. Before measurements, all devices were stored in the glovebox and tested under the ambient atmosphere without encapsulation.

LED Performance Characterization. A Keithley 2400 source meter was used to measure the current density−voltage (J−V) characteristics. The EL spectra were recorded through an optical fiber by using a calibrated LR1 compact spectrometer (ASEQ Instruments) with thermoelectric cooling and a spectral range of 300 to 1000 nm. A spectroradiometer (Photoresearch PR-655) was used to calibrate the LR1 spectrometer. The photon flux was measured using an optical power meter (PM12 VA from Thorlabs) with a calibrated silicon photodiode detector. The EQE was calculated as the total number of emitted photons divided by the total number of injected electrons by assuming a Lambertian emission profile.

UV−Vis Absorbance. Spectra were recorded with a Jasco V670 spectrometer in transmission mode.

Steady-State Photoluminescence. PL spectra were collected using a Fluorolog iHR 320 Horiba Jobin Yvon spectrometer equipped with a PMT detector. The PL QYs of the colloidal hexane solutions were determined using standard procedures. The following dye molecules were used as references: HITCI for $FAPbI_3$ NCs and oxazine 1 for (FA/Cs)PbI_3 NCs (Figure S8).[170,171]

Time-Resolved Photoluminescence. These measurements were performed using a time-correlated single photon counting system equipped with the SPC-130-EM counting module (Becker & Hickl GmbH) and an IDQ-ID-100-20-ULN avalanche photodiode (Quantique) for recording the decay traces. Emissions from the perovskite NCs were excited by using a BDL-488-SMN laser (Becker & Hickl) with a pulse duration of 50 ps, a wavelength of 488 nm, and a CW power equivalent of ∼0.5 mW and were externally triggered at a repetition rate of 1 MHz. PL emissions from the samples were passed through a long-pass optical filter with an edge at 500 nm to reject the excitation laser line.

Photoluminescence Quantum Yield (PL QY) Measurements of Films. The method used to measure the absolute value of the PL QY was similar to the method used by Semonin *et al.*[172] An integrating sphere (IS200-4, Thorlabs) with a short-pass filter (FES450, Thorlabs) was used, the absorbance was corrected to the reflectance, and the scattering losses were estimated. A CW laser diode with a wavelength of 405 nm and a power of 0.2 W modulated at 30 Hz was used as the excitation source. The amounts of emitted light were measured using long-pass filters (FEL450, Thorlabs). The light intensity was measured using a broadband (0.1−20 μm) UM9B-BL-DA pyroelectric photodetector (Gentec-EO). The modulated signal from the detector was recovered by using a lock-in amplifier (SR 850, Stanford Research). The ratio between the emitted and absorbed light gives the energy yield. The PL QY was obtained from the value of an energy yield and corrected to the ratio of the photon energies of the laser beam and PL bands.

Amplified Spontaneous Emission. ASE measurements were performed using excitation from a femtosecond laser system consisting of an oscillator (Vitesse 800) and an amplifier (Legend Elite), which were both from Coherent Inc., and a frequency-doubling external BBO crystal that yielded 100 fs pulses at 400 nm, a repetition rate of 1 kHz, and a pulse energy of up to 4 μJ. The laser beam profile had a TEM00 mode with a fwhm of 1.5 mm. The laser power was measured by using a LabMax-TOP laser energy meter (Coherent Inc.) with a nJ measuring head. The optical emissions were recorded by using the LR1-T CCD spectrometer of the ASEQ-instrument (1 nm spectral resolution). The laser beam intensity profiles were determined by using a LabMax-TOP camera from Coherent Inc.

Powder X-ray Diffraction Patterns. XRD was recorded using a powder diffractometer (STOE STADI P) with Cu $K\alpha_1$ radiation. The

DOI: 10.1021/acsnano.7b00116
ACS Nano 2017, 11, 3119−3134

diffractometer was operated in transmission mode and included a germanium monochromator and a silicon strip detector (Dectris Mythen).

Synchrotron X-ray Total Scattering Measurements. Colloidal suspensions of $FAPbI_3$ and $FA_{0.1}Cs_{0.9}PbI_3$ were loaded into 0.8-mm-diameter certified borosilicate glass capillaries. Synchrotron X-ray total scattering measurements were conducted at the X04SA-MS4 Powder Diffraction Beamline of the Swiss Light Source (Paul Scherrer Institute, Villigen, Switzerland).[151] The operational beam energy was set at 22 keV (λ = 0.565 483 Å) and was accurately determined using a silicon powder standard (NIST 640d, a_0 = 0.543123(8) nm at 22.5 °C). Data were collected from 0.5° to 130° 2θ using a single-photon counting silicon microstrip detector (MYTHEN II).[173] Using a He/air background, the scattering patterns of the empty glass capillary tubes and pure solvent were independently collected under the same experimental conditions and then subtracted from the sample signals. The transmission coefficients of the sample and solvent-loaded capillaries were also measured and used for the angle-dependent absorption correction. Instead of being subtracted, the inelastic Compton scattering was added as an additional model component during the data analysis. For the DFA, the 3−100° angular range was used.

Transmission Electron Microscopy. TEM images were recorded using a JEOL JEM-2200FS microscope operated at 200 kV.

Rutherford Backscattering Spectrometry. RBS was conducted at the ETH Laboratory for Ion Beam Physics by using a 2 MeV ^{4}He beam and a silicon PIN diode detector at 168°. The resulting data were evaluated by using the RUMP code.[174]

Energy-Dispersive X-ray Spectroscopy. EDX was performed using a Zeiss Gemini 1530/Hitachi S-4800 scanning electron microscope.

ASSOCIATED CONTENT

Supporting Information

The Supporting Information is available free of charge on the ACS Publications website at DOI: 10.1021/acsnano.7b00116.

Details of the DSE analysis and additional figures characterizing the materials (PDF)

AUTHOR INFORMATION

Corresponding Author

*E-mail: mvkovalenko@ethz.ch.

ORCID

Sergii Yakunin: 0000-0002-6409-0565
Federica Bertolotti: 0000-0002-6001-9040
Norberto Masciocchi: 0000-0001-9921-2350
Antonietta Guagliardi: 0000-0001-6390-2114
Chih-Jen Shih: 0000-0002-5258-3485
Maksym V. Kovalenko: 0000-0002-6396-8938

Notes

The authors declare no competing financial interest.

ACKNOWLEDGMENTS

This work was financially supported by the European Union through the FP7 (ERC Starting Grant NANOSOLID, GA No. 306733) and in part by the Swiss Federal Commission for Technology and Innovation (CTI-No. 18614.1 PFNM-NM). M.B. is grateful to the Swiss National Science Foundation for an Ambizione Energy fellowship (Grant No. PZENP2_154287). The authors thank Dr. Max Döbeli for conducting the RBS measurements, Dr. Frank Krumeich for conducting the EDX measurements, Dr. Stefan Günther for assistance with the fs-laser source, Dr. Antonio Cervellino and the staff at the X04SA-MS beamline of the SLS for their technical support, and Nadia Schwitz for obtaining the photographs. The authors are grateful to the research facilities of ETH Zürich (FIRST, Center for Micro- and Nanoscience and ScopeM, Scientific Center for Optical and Electron Microscopy) and Empa (Empa Electron Microscopy Center) for allowing the use of necessary instruments and for technical assistance.

REFERENCES

(1) Kim, H.-S.; Lee, C.-R.; Im, J.-H.; Lee, K.-B.; Moehl, T.; Marchioro, A.; Moon, S.-J.; Humphry-Baker, R.; Yum, J.-H.; Moser, J. E.; Grätzel, M.; Park, N.-G. Lead Iodide Perovskite Sensitized All-Solid-State Submicron Thin Film Mesoscopic Solar Cell with Efficiency Exceeding 9%. *Sci. Rep.* **2012**, *2*, 591.

(2) Lee, M. M.; Teuscher, J.; Miyasaka, T.; Murakami, T. N.; Snaith, H. J. Efficient Hybrid Solar Cells Based on Meso-Superstructured Organometal Halide Perovskites. *Science* **2012**, *338*, 643−647.

(3) Research Cell Efficiency Records. http://www.Nrel.Gov/Ncpv/Images/Efficiency_Chart.Jpg (accessed May 2016).

(4) Saliba, M.; Matsui, T.; Domanski, K.; Seo, J.-Y.; Ummadisingu, A.; Zakeeruddin, S. M.; Correa-Baena, J.-P.; Tress, W. R.; Abate, A.; Hagfeldt, A.; Grätzel, M. Incorporation of Rubidium Cations into Perovskite Solar Cells Improves Photovoltaic Performance. *Science* **2016**, *354*, 206−209.

(5) Brivio, F.; Frost, J. M.; Skelton, J. M.; Jackson, A. J.; Weber, O. J.; Weller, M. T.; Goñi, A. R.; Leguy, A. M. A.; Barnes, P. R. F.; Walsh, A. Lattice Dynamics and Vibrational Spectra of the Orthorhombic, Tetragonal, and Cubic Phases of Methylammonium Lead Iodide. *Phys. Rev. B: Condens. Matter Mater. Phys.* **2015**, *92*, 144308.

(6) Yang, T.-Y.; Gregori, G.; Pellet, N.; Grätzel, M.; Maier, J. The Significance of Ion Conduction in a Hybrid Organic−Inorganic Lead-Iodide-Based Perovskite Photosensitizer. *Angew. Chem., Int. Ed.* **2015**, *54*, 7905−7910.

(7) Mosconi, E.; De Angelis, F. Mobile Ions in Organohalide Perovskites: Interplay of Electronic Structure and Dynamics. *ACS Energy Lett.* **2016**, *1*, 182−188.

(8) Zakutayev, A.; Caskey, C. M.; Fioretti, A. N.; Ginley, D. S.; Vidal, J.; Stevanovic, V.; Tea, E.; Lany, S. Defect Tolerant Semiconductors for Solar Energy Conversion. *J. Phys. Chem. Lett.* **2014**, *5*, 1117−1125.

(9) Brandt, R. E.; Stevanović, V.; Ginley, D. S.; Buonassisi, T. Identifying Defect-Tolerant Semiconductors With High Minority-Carrier Lifetimes: Beyond Hybrid Lead Halide Perovskites. *MRS Commun.* **2015**, *5*, 265−275.

(10) Manser, J. S.; Christians, J. A.; Kamat, P. V. Intriguing Optoelectronic Properties of Metal Halide Perovskites. *Chem. Rev.* **2016**, *116*, 12956−13008.

(11) Shi, D.; Adinolfi, V.; Comin, R.; Yuan, M.; Alarousu, E.; Buin, A.; Chen, Y.; Hoogland, S.; Rothenberger, A.; Katsiev, K.; Losovyj, Y.; Zhang, X.; Dowben, P. A.; Mohammed, O. F.; Sargent, E. H.; Bakr, O. M. Low Trap-State Density and Long Carrier Diffusion in Organolead Trihalide Perovskite Single Crystals. *Science* **2015**, *347*, 519−522.

(12) Zhumekenov, A. A.; Saidaminov, M. I.; Haque, M. A.; Alarousu, E.; Sarmah, S. P.; Murali, B.; Dursun, I.; Miao, X.-H.; Abdelhady, A. L.; Wu, T.; Mohammed, O. F.; Bakr, O. M. Formamidinium Lead Halide Perovskite Crystals with Unprecedented Long Carrier Dynamics and Diffusion Length. *ACS Energy Lett.* **2016**, *1*, 32−37.

(13) Lian, Z.; Yan, Q.; Gao, T.; Ding, J.; Lv, Q.; Ning, C.; Li, Q.; Sun, J.-l. Perovskite $CH_3NH_3PbI_3$(Cl) Single Crystals: Rapid Solution Growth, Unparalleled Crystalline Quality, and Low Trap Density toward 108 cm^{-3}. *J. Am. Chem. Soc.* **2016**, *138*, 9409−9412.

(14) Stoumpos, C. C.; Malliakas, C. D.; Peters, J. A.; Liu, Z.; Sebastian, M.; Im, J.; Chasapis, T. C.; Wibowo, A. C.; Chung, D. Y.; Freeman, A. J.; Wessels, B. W.; Kanatzidis, M. G. Crystal Growth of the Perovskite Semiconductor $CsPbBr_3$: A New Material for High-Energy Radiation Detection. *Cryst. Growth Des.* **2013**, *13*, 2722−2727.

(15) Maculan, G.; Sheikh, A. D.; Abdelhady, A. L.; Saidaminov, M. I.; Haque, M. A.; Murali, B.; Alarousu, E.; Mohammed, O. F.; Wu, T.; Bakr, O. M. $CH_3NH_3PbCl_3$ Single Crystals: Inverse Temperature

DOI: 10.1021/acsnano.7b00116
ACS Nano 2017, 11, 3119−3134

Crystallization and Visible-Blind UV-Photodetector. *J. Phys. Chem. Lett.* **2015**, *6*, 3781−3786.
(16) Saidaminov, M. I.; Abdelhady, A. L.; Murali, B.; Alarousu, E.; Burlakov, V. M.; Peng, W.; Dursun, I.; Wang, L.; He, Y.; Maculan, G.; Goriely, A.; Wu, T.; Mohammed, O. F.; Bakr, O. M. High-Quality Bulk Hybrid Perovskite Single Crystals Within Minutes by Inverse Temperature Crystallization. *Nat. Commun.* **2015**, *6*, 7586.
(17) Miyata, A.; Mitioglu, A.; Plochocka, P.; Portugall, O.; Wang, J. T.-W.; Stranks, S. D.; Snaith, H. J.; Nicholas, R. J. Direct Measurement of the Exciton Binding Energy and Effective Masses for Charge Carriers in Organic-Inorganic Tri-Halide Perovskites. *Nat. Phys.* **2015**, *11*, 582−587.
(18) Dou, L.; Yang, Y.; You, J.; Hong, Z.; Chang, W.-H.; Li, G.; Yang, Y. Solution-Processed Hybrid Perovskite Photodetectors with High Detectivity. *Nat. Commun.* **2014**, *5*, 5404.
(19) Fang, Y.; Dong, Q.; Shao, Y.; Yuan, Y.; Huang, J. Highly Narrowband Perovskite Single-Crystal Photodetectors Enabled by Surface-Charge Recombination. *Nat. Photonics* **2015**, *9*, 679−686.
(20) Saidaminov, M. I.; Adinolfi, V.; Comin, R.; Abdelhady, A. L.; Peng, W.; Dursun, I.; Yuan, M.; Hoogland, S.; Sargent, E. H.; Bakr, O. M. Planar-Integrated Single-Crystalline Perovskite Photodetectors. *Nat. Commun.* **2015**, *6*, 8724.
(21) Yakunin, S.; Sytnyk, M.; Kriegner, D.; Shrestha, S.; Richter, M.; Matt, G. J.; Azimi, H.; Brabec, C. J.; Stangl, J.; Kovalenko, M. V.; Heiss, W. Detection of X-ray Photons by Solution-Processed Lead Halide Perovskites. *Nat. Photonics* **2015**, *9*, 444−449.
(22) Wei, H.; Fang, Y.; Mulligan, P.; Chuirazzi, W.; Fang, H.-H.; Wang, C.; Ecker, B. R.; Gao, Y.; Loi, M. A.; Cao, L.; Huang, J. Sensitive X-ray Detectors Made of Methylammonium Lead Tribromide Perovskite Single Crystals. *Nat. Photonics* **2016**, *10*, 333−339.
(23) Dong, Q.; Fang, Y.; Shao, Y.; Mulligan, P.; Qiu, J.; Cao, L.; Huang, J. Electron-Hole Diffusion Lengths > 175 μm in Solution-Grown $CH_3NH_3PbI_3$ Single Crystals. *Science* **2015**, *347*, 967−970.
(24) Bai, Z.; Zhong, H. Halide Perovskite Quantum Dots: Potential Candidates for Display Technology. *Sci. Bull.* **2015**, *60*, 1622−1624.
(25) Yoon, H. C.; Kang, H.; Lee, S.; Oh, J. H.; Yang, H.; Do, Y. R. Study of Perovskite QD Down-Converted LEDs and Six-Color White LEDs for Future Displays with Excellent Color Performance. *ACS Appl. Mater. Interfaces* **2016**, *8*, 18189−18200.
(26) Stranks, S. D.; Snaith, H. J. Metal-Halide Perovskites for Photovoltaic and Light-Emitting Devices. *Nat. Nanotechnol.* **2015**, *10*, 391−402.
(27) Tan, Z.-K.; Moghaddam, R. S.; Lai, M. L.; Docampo, P.; Higler, R.; Deschler, F.; Price, M.; Sadhanala, A.; Pazos, L. M.; Credgington, D.; Hanusch, F.; Bein, T.; Snaith, H. J.; Friend, R. H. Bright Light-Emitting Diodes Based on Organometal Halide Perovskite. *Nat. Nanotechnol.* **2014**, *9*, 687−692.
(28) Jaramillo-Quintero, O. A.; Sanchez, R. S.; Rincon, M.; Mora-Sero, I. Bright Visible-Infrared Light Emitting Diodes Based on Hybrid Halide Perovskite with Spiro-OMeTAD as a Hole-Injecting Layer. *J. Phys. Chem. Lett.* **2015**, *6*, 1883−1890.
(29) Kim, Y. H.; Cho, H.; Heo, J. H.; Kim, T. S.; Myoung, N.; Lee, C. L.; Im, S. H.; Lee, T. W. Multicolored Organic/Inorganic Hybrid Perovskite Light-Emitting Diodes. *Adv. Mater.* **2015**, *27*, 1248−1254.
(30) Zhang, X.; Sun, C.; Zhang, Y.; Wu, H.; Ji, C.; Chuai, Y.; Wang, P.; Wen, S.; Zhang, C.; Yu, W. W. Bright Perovskite Nanocrystal Films for Efficient Light-Emitting Devices. *J. Phys. Chem. Lett.* **2016**, *7*, 4602−4610.
(31) Byun, J.; Cho, H.; Wolf, C.; Jang, M.; Sadhanala, A.; Friend, R. H.; Yang, H.; Lee, T.-W. Efficient Visible Quasi-2D Perovskite Light-Emitting Diodes. *Adv. Mater.* **2016**, *28*, 7515−7520.
(32) Cho, H.; Jeong, S.-H.; Park, M.-H.; Kim, Y.-H.; Wolf, C.; Lee, C.-L.; Heo, J. H.; Sadhanala, A.; Myoung, N.; Yoo, S.; Im, S. H.; Friend, R. H.; Lee, T.-W. Overcoming the Electroluminescence Efficiency Limitations of Perovskite Light-Emitting Diodes. *Science* **2015**, *350*, 1222−1225.
(33) Kim, Y.-H.; Cho, H.; Lee, T.-W. Metal Halide Perovskite Light Emitters. *Proc. Natl. Acad. Sci. U. S. A.* **2016**, *113*, 11694−11702.
(34) Xing, G.; Mathews, N.; Lim, S. S.; Yantara, N.; Liu, X.; Sabba, D.; Grätzel, M.; Mhaisalkar, S.; Sum, T. C. Low-Temperature Solution-Processed Wavelength-Tunable Perovskites for Lasing. *Nat. Mater.* **2014**, *13*, 476−480.
(35) Zhu, H.; Fu, Y.; Meng, F.; Wu, X.; Gong, Z.; Ding, Q.; Gustafsson, M. V.; Trinh, M. T.; Jin, S.; Zhu, X. Y. Lead Halide Perovskite Nanowire Lasers with Low Lasing Thresholds and High Quality Factors. *Nat. Mater.* **2015**, *14*, 636−642.
(36) Yakunin, S.; Protesescu, L.; Krieg, F.; Bodnarchuk, M. I.; Nedelcu, G.; Humer, M.; De Luca, G.; Fiebig, M.; Heiss, W.; Kovalenko, M. V. Low-Threshold Amplified Spontaneous Emission and Lasing from Colloidal Nanocrystals of Caesium Lead Halide Perovskites. *Nat. Commun.* **2015**, *6*, 8056.
(37) Protesescu, L.; Yakunin, S.; Bodnarchuk, M. I.; Krieg, F.; Caputo, R.; Hendon, C. H.; Yang, R. X.; Walsh, A.; Kovalenko, M. V. Nanocrystals of Cesium Lead Halide Perovskites ($CsPbX_3$, X = Cl, Br, and I): Novel Optoelectronic Materials Showing Bright Emission with Wide Color Gamut. *Nano Lett.* **2015**, *15*, 3692−3696.
(38) Zhang, F.; Zhong, H.; Chen, C.; Wu, X.-g.; Hu, X.; Huang, H.; Han, J.; Zou, B.; Dong, Y. Brightly Luminescent and Color-Tunable Colloidal $CH_3NH_3PbX_3$ (X = Br, I, Cl) Quantum Dots: Potential Alternatives for Display Technology. *ACS Nano* **2015**, *9*, 4533−4542.
(39) Schmidt, L. C.; Pertegás, A.; González-Carrero, S.; Malinkiewicz, O.; Agouram, S.; Mínguez Espallargas, G.; Bolink, H. J.; Galian, R. E.; Pérez-Prieto, J. Nontemplate Synthesis of $CH_3NH_3PbBr_3$ Perovskite Nanoparticles. *J. Am. Chem. Soc.* **2014**, *136*, 850−853.
(40) Gonzalez-Carrero, S.; Galian, R. E.; Perez-Prieto, J. Maximizing the Emissive Properties of $CH_3NH_3PbBr_3$ Perovskite Nanoparticles. *J. Mater. Chem. A* **2015**, *3*, 9187−9193.
(41) Horváth, E.; Spina, M.; Szekrényes, Z.; Kamarás, K.; Gaal, R.; Gachet, D.; Forró, L. Nanowires of Methylammonium Lead Iodide ($CH_3NH_3PbI_3$) Prepared by Low Temperature Solution-Mediated Crystallization. *Nano Lett.* **2014**, *14*, 6761−6766.
(42) Tyagi, P.; Arveson, S. M.; Tisdale, W. A. Colloidal Organohalide Perovskite Nanoplatelets Exhibiting Quantum Confinement. *J. Phys. Chem. Lett.* **2015**, *6*, 1911−1916.
(43) Jang, D. M.; Park, K.; Kim, D. H.; Park, J.; Shojaei, F.; Kang, H. S.; Ahn, J. P.; Lee, J. W.; Song, J. K. Reversible Halide Exchange Reaction of Organometal Trihalide Perovskite Colloidal Nanocrystals for Full-Range Band Gap Tuning. *Nano Lett.* **2015**, *15*, 5191−5199.
(44) Huang, H.; Susha, A. S.; Kershaw, S. V.; Hung, T. F.; Rogach, A. L. Control of Emission Color of High Quantum Yield $CH_3NH_3PbBr_3$ Perovskite Quantum Dots by Precipitation Temperature. *Adv. Sci.* **2015**, *2*, 1500194.
(45) Wong, A. B.; Lai, M.; Eaton, S. W.; Yu, Y.; Lin, E.; Dou, L.; Fu, A.; Yang, P. Growth and Anion Exchange Conversion of $CH_3NH_3PbX_3$ Nanorod Arrays for Light-Emitting Diodes. *Nano Lett.* **2015**, *15*, 5519−5524.
(46) Sichert, J. A.; Tong, Y.; Mutz, N.; Vollmer, M.; Fischer, S.; Milowska, K. Z.; García Cortadella, R.; Nickel, B.; Cardenas-Daw, C.; Stolarczyk, J. K.; Urban, A. S.; Feldmann, J. Quantum Size Effect in Organometal Halide Perovskite Nanoplatelets. *Nano Lett.* **2015**, *15*, 6521−6527.
(47) Dou, L.; Wong, A. B.; Yu, Y.; Lai, M.; Kornienko, N.; Eaton, S. W.; Fu, A.; Bischak, C. G.; Ma, J.; Ding, T.; Ginsberg, N. S.; Wang, L.-W.; Alivisatos, A. P.; Yang, P. Atomically Thin Two-Dimensional Organic-Inorganic Hybrid Perovskites. *Science* **2015**, *349*, 1518−1521.
(48) Hassan, Y.; Song, Y.; Pensack, R. D.; Abdelrahman, A. I.; Kobayashi, Y.; Winnik, M. A.; Scholes, G. D. Structure-Tuned Lead Halide Perovskite Nanocrystals. *Adv. Mater.* **2016**, *28*, 566−573.
(49) Vybornyi, O.; Yakunin, S.; Kovalenko, M. V. Polar-Solvent-Free Colloidal Synthesis of Highly Luminescent Alkylammonium Lead Halide Perovskite Nanocrystals. *Nanoscale* **2016**, *8*, 6278−6283.
(50) Huang, S.; Li, Z.; Kong, L.; Zhu, N.; Shan, A.; Li, L. Enhancing the Stability of $CH_3NH_3PbBr_3$ Quantum Dots by Embedding in Silica Spheres Derived from Tetramethyl Orthosilicate in "Waterless" Toluene. *J. Am. Chem. Soc.* **2016**, *138*, 5749−5752.

DOI: 10.1021/acsnano.7b00116
ACS Nano 2017, 11, 3119−3134

(51) Aharon, S.; Etgar, L. Two Dimensional Organometal Halide Perovskite Nanorods with Tunable Optical Properties. *Nano Lett.* **2016**, *16*, 3230−3235.
(52) Ha, S. T.; Liu, X.; Zhang, Q.; Giovanni, D.; Sum, T. C.; Xiong, Q. Synthesis of Organic-Inorganic Lead Halide Perovskite Nanoplatelets: Towards High-Performance Perovskite Solar Cells and Optoelectronic Devices. *Adv. Opt. Mater.* **2014**, *2*, 838−844.
(53) Di, D.; Musselman, K. P.; Li, G.; Sadhanala, A.; Ievskaya, Y.; Song, Q.; Tan, Z. K.; Lai, M. L.; MacManus-Driscoll, J. L.; Greenham, N. C.; Friend, R. H. Size-Dependent Photon Emission from Organometal Halide Perovskite Nanocrystals Embedded in an Organic Matrix. *J. Phys. Chem. Lett.* **2015**, *6*, 446−450.
(54) Fu, Y.; Meng, F.; Rowley, M. B.; Thompson, B. J.; Shearer, M. J.; Ma, D.; Hamers, R. J.; Wright, J. C.; Jin, S. Solution Growth of Single Crystal Methylammonium Lead Halide Perovskite Nanostructures for Optoelectronic and Photovoltaic Applications. *J. Am. Chem. Soc.* **2015**, *137*, 5810−5818.
(55) Hines, M. A.; Guyot-Sionnest, P. Synthesis and Characterization of Strongly Luminescing ZnS-Capped CdSe Nanocrystals. *J. Phys. Chem.* **1996**, *100*, 468−471.
(56) Cao, Y.-W.; Banin, U. Synthesis and Characterization of InAs/InP and InAs/CdSe Core/Shell Nanocrystals. *Angew. Chem., Int. Ed.* **1999**, *38*, 3692−3694.
(57) Mićić, O. I.; Smith, B. B.; Nozik, A. J. Core−Shell Quantum Dots of Lattice-Matched ZnCdSe2 Shells on InP Cores: Experiment and Theory. *J. Phys. Chem. B* **2000**, *104*, 12149−12156.
(58) Yassitepe, E. Amine-Free Synthesis of Cesium Lead Halide Perovskite Quantum Dots for Efficient Light-Emitting Diodes. *Adv. Funct. Mater.* **2016**, *26*, 8757−8763.
(59) Sun, S. Ligand-Mediated Synthesis of Shape-Controlled Cesium Lead Halide Perovskite Nanocrystals via Reprecipitation Process at Room Temperature. *ACS Nano* **2016**, *10*, 3648−3657.
(60) Zhang, D. Solution-Phase Synthesis of Cesium Lead Halide Perovskite Nanowires. *J. Am. Chem. Soc.* **2015**, *137*, 9230−9233.
(61) Bekenstein, Y. Highly Luminescent Colloidal Nanoplates of Perovskite Cesium Lead Halide and Their Oriented Assemblies. *J. Am. Chem. Soc.* **2015**, *137*, 16008−16011.
(62) Akkerman, Q. Synthesis Approach to Colloidal Cesium Lead Halide Perovskite 40 Nanoplatelets with Monolayer-Level Thickness Control. *J. Am. Chem. Soc.* **2016**, *138*, 1010−1016.
(63) Shamsi, J. Colloidal Synthesis of Quantum Confined Single Crystal CsPbBr3 Nanosheets with Lateral Size Control up to the Micrometer Range. *J. Am. Chem. Soc.* **2016**, *138*, 7240−7243.
(64) Nedelcu, G. Fast Anion-Exchange in Highly Luminescent Nanocrystals of Cesium Lead Halide Perovskites (CsPbX 3 , X = Cl, Br, I). *Nano Lett.* **2015**, *15*, 5635−5640.
(65) Akkerman, Q. Tuning the Optical Properties of Cesium Lead Halide Perovskite Nanocrystals by Anion Exchange Reactions. *J. Am. Chem. Soc.* **2015**, *137*, 10276−10281.
(66) Zhang, D. Synthesis of Composition Tunable and Highly Luminescent Cesium Lead Halide Nanowires through Anion-Exchange Reactions. *J. Am. Chem. Soc.* **2016**, *138*, 7236−7239.
(67) Koolyk, M. Kinetics of Cesium Lead Halide Perovskite Nanoparticle Growth; Focusing and de-Focusing of Size Distribution. *Nanoscale* **2016**, *8*, 6403−6409.
(68) Lignos, I. Synthesis of Cesium Lead Halide Perovskite Nanocrystals in a Droplet-Based Microfluidic Platform: Fast Parametric Space Mapping. *Nano Lett.* **2016**, *16*, 1869−1877.
(69) Chen, X. Non-Injection Gram-Scale Synthesis of Cesium Lead Halide Perovskite Quantum Dots with Controllable Size and Composition. *Nano Res.* **2016**, *9*, 1−13.
(70) Ramasamy, P. All-Inorganic Cesium Lead Halide Perovskite Nanocrystals for Photodetector Applications. *Chem. Commun.* **2016**, *52*, 2067−2070.
(71) Zhang, D. Ultrathin Colloidal Cesium Lead Halide Perovskite Nanowires. *J. Am. Chem. Soc.* **2016**, *138*, 13155−13158.
(72) Zhang, X. Self-Assembly of One-Dimensional Nanocrystal Superlattice Chains Mediated by Molecular Clusters. *J. Am. Chem. Soc.* **2016**, *138*, 3290−3293.
(73) Palazon, F. X-ray Lithography on Perovskite Nanocrystals Films: From Patterning with Anion-Exchange Reactions to Enhanced Stability in Air and Water. *ACS Nano* **2016**, *10*, 1224−1230.
(74) Tong, Y. Highly Luminescent Cesium Lead Halide Perovskite Nanocrystals with Tunable Composition and Thickness by Ultrasonication. *Angew. Chem., Int. Ed.* **2016**, *55*, 13887−13892.
(75) Kim, Y. Efficient Luminescence from Perovskite Quantum Dot Solids. *ACS Appl. Mater. Interfaces* **2015**, *7*, 25007−25013.
(76) De Roo, J.; Ibáñez, M.; Geiregat, P.; Nedelcu, G.; Walravens, W.; Maes, J.; Martins, J. C.; Van Driessche, I.; Kovalenko, M. V.; Hens, Z. Highly Dynamic Ligand Binding and Light Absorption Coefficient of Cesium Lead Bromide Perovskite Nanocrystals. *ACS Nano* **2016**, *10*, 2071−2081.
(77) Huang, H.; Chen, B.; Wang, Z.; Hung, T. F.; Susha, A. S.; Zhong, H.; Rogach, A. L. Water Resistant $CsPbX_3$ Nanocrystals Coated with Polyhedral Oligomeric Silsesquioxane and Their Use as Solid State Luminophores in All-Perovskite White Light-Emitting Devices. *Chem. Sci.* **2016**, *7*, 5699−5703.
(78) Guo, Y.; Shoyama, K.; Sato, W.; Nakamura, E. Polymer Stabilization of Lead(II) Perovskite Cubic Nanocrystals for Semitransparent Solar Cells. *Adv. Energy Mater.* **2016**, *6*, 1502317.
(79) Pan, J.; Quan, L. N.; Zhao, Y.; Peng, W.; Murali, B.; Sarmah, S. P.; Yuan, M.; Sinatra, L.; Alyami, N. M.; Liu, J.; Yassitepe, E.; Yang, Z.; Voznyy, O.; Comin, R.; Hedhili, M. N.; Mohammed, O. F.; Lu, Z. H.; Kim, D. H.; Sargent, E. H.; Bakr, O. M. Highly Efficient Perovskite-Quantum-Dot Light-Emitting Diodes by Surface Engineering. *Adv. Mater.* **2016**, *28*, 8718−8725.
(80) Pan, J.; Sarmah, S. P.; Murali, B.; Dursun, I.; Peng, W.; Parida, M. R.; Liu, J.; Sinatra, L.; Alyami, N.; Zhao, C.; Alarousu, E.; Ng, T. K.; Ooi, B. S.; Bakr, O. M.; Mohammed, O. F. Air-Stable Surface-Passivated Perovskite Quantum Dots for Ultra-Robust, Single- and Two-Photon-Induced Amplified Spontaneous Emission. *J. Phys. Chem. Lett.* **2015**, *6*, 5027−5033.
(81) Yu, Y.; Zhang, D.; Kisielowski, C.; Dou, L.; Kornienko, N.; Bekenstein, Y.; Wong, A. B.; Alivisatos, A. P.; Yang, P. Atomic Resolution Imaging of Halide Perovskites. *Nano Lett.* **2016**, *16*, 7530.
(82) Cottingham, P.; Brutchey, R. L. Compositionally Dependent Phase Identity of Colloidal $CsPbBr_{3-x}I_x$ Quantum Dots. *Chem. Mater.* **2016**, *28*, 7574−7577.
(83) Cottingham, P.; Brutchey, R. L. On the Crystal Structure of Colloidally Prepared $CsPbBr_3$ Quantum Dots. *Chem. Commun.* **2016**, *52*, 5246−5249.
(84) Tian, Y.; Merdasa, A.; Peter, M.; Abdellah, M.; Zheng, K.; Ponseca, C. S.; Pullerits, T.; Yartsev, A.; Sundström, V.; Scheblykin, I. G. Giant Photoluminescence Blinking of Perovskite Nanocrystals Reveals Single-Trap Control of Luminescence. *Nano Lett.* **2015**, *15*, 1603−1608.
(85) Park, Y. S.; Guo, S.; Makarov, N. S.; Klimov, V. I. Room Temperature Single-Photon Emission from Individual Perovskite Quantum Dots. *ACS Nano* **2015**, *9*, 10386−10393.
(86) Swarnkar, A.; Chulliyil, R.; Ravi, V. K.; Irfanullah, M.; Chowdhury, A.; Nag, A. Colloidal $CsPbBr_3$ Perovskite Nanocrystals: Luminescence beyond Traditional Quantum Dots. *Angew. Chem., Int. Ed.* **2015**, *54*, 15424−15428.
(87) Hu, F.; Zhang, H.; Sun, C.; Yin, C.; Lv, B.; Zhang, C.; Yu, W. W.; Wang, X.; Zhang, Y.; Xiao, M. Superior Optical Properties of Perovskite Nanocrystals as Single Photon Emitters. *ACS Nano* **2015**, *9*, 12410−12416.
(88) Makarov, N. S.; Guo, S.; Isaienko, O.; Liu, W.; Robel, I.; Klimov, V. I. Spectral and Dynamical Properties of Single Excitons, Biexcitons, and Trions in Cesium-Lead-Halide Perovskite Quantum Dots. *Nano Lett.* **2016**, *16*, 2349−2362.
(89) Rainò, G.; Nedelcu, G.; Protesescu, L.; Bodnarchuk, M. I.; Kovalenko, M. V.; Mahrt, R. F.; Stöferle, T. Single Cesium Lead Halide Perovskite Nanocrystals at Low Temperature: Fast Single-Photon Emission, Reduced Blinking, and Exciton Fine Structure. *ACS Nano* **2016**, *10*, 2485−2490.
(90) Wang, Y.; Li, X.; Zhao, X.; Xiao, L.; Zeng, H.; Sun, H. Nonlinear Absorption and Low-Threshold Multiphoton Pumped Stimulated

DOI: 10.1021/acsnano.7b00116
ACS Nano 2017, 11, 3119−3134

Emission from All-Inorganic Perovskite Nanocrystals. *Nano Lett.* **2016**, *16*, 448−453.
(91) Xie, B.; Hu, R.; Luo, X. Quantum Dots-Converted Light-Emitting Diodes Packaging for Lighting and Display: Status and Perspectives. *J. Electron. Packag.* **2016**, *138*, 020803−020816.
(92) Zhang, X.; Wang, H.-C.; Tang, A.-C.; Lin, S.-Y.; Tong, H.-C.; Chen, C.-Y.; Lee, Y.-C.; Tsai, T.-L.; Liu, R.-S. Robust and Stable Narrow-Band Green Emitter: An Option for Advanced Wide-Color-Gamut Backlight Display. *Chem. Mater.* **2016**, *28*, 8493.
(93) Wang, H.-C.; Lin, S.-Y.; Tang, A.-C.; Singh, B. P.; Tong, H.-C.; Chen, C.-Y.; Lee, Y.-C.; Tsai, T.-L.; Liu, R.-S. Mesoporous Silica Particles Integrated with All-Inorganic $CsPbBr_3$ Perovskite Quantum-Dot Nanocomposites (MP-PQDs) with High Stability and Wide Color Gamut Used for Backlight Display. *Angew. Chem., Int. Ed.* **2016**, *55*, 7924−7929.
(94) Oh, J. H.; Eo, Y. J.; Yoon, H. C.; Huh, Y.-D.; Do, Y. R. Evaluation of New Color Metrics: Guidelines for Developing Narrow-Band Red Phosphors for WLEDs. *J. Mater. Chem. C* **2016**, *4*, 8326−8348.
(95) Song, J.; Li, J.; Li, X.; Xu, L.; Dong, Y.; Zeng, H. Quantum Dot Light-Emitting Diodes Based on Inorganic Perovskite Cesium Lead Halides ($CsPbX_3$). *Adv. Mater.* **2015**, *27*, 7162−7167.
(96) Zhang, X.; Lin, H.; Huang, H.; Reckmeier, C.; Zhang, Y.; Choy, W. C. H.; Rogach, A. L. Enhancing the Brightness of Cesium Lead Halide Perovskite Nanocrystal Based Green Light-Emitting Devices through the Interface Engineering with Perfluorinated Ionomer. *Nano Lett.* **2016**, *16*, 1415−1420.
(97) Li, G.; Rivarola, F. W. R.; Davis, N. J. L. K.; Bai, S.; Jellicoe, T. C.; de la Peña, F.; Hou, S.; Ducati, C.; Gao, F.; Friend, R. H.; Greenham, N. C.; Tan, Z.-K. Highly Efficient Perovskite Nanocrystal Light-Emitting Diodes Enabled by a Universal Crosslinking Method. *Adv. Mater.* **2016**, *28*, 3528−3534.
(98) Zhang, X.; Xu, B.; Zhang, J.; Gao, Y.; Zheng, Y.; Wang, K.; Sun, X. W. All-Inorganic Perovskite Nanocrystals for High-Efficiency Light Emitting Diodes: Dual-Phase $CsPbBr_3$-$CsPb_2Br_5$ Composites. *Adv. Funct. Mater.* **2016**, *26*, 1616−3026.
(99) Swarnkar, A.; Marshall, A. R.; Sanehira, E. M.; Chernomordik, B. D.; Moore, D. T.; Christians, J. A.; Chakrabarti, T.; Luther, J. M. Quantum Dot−Induced Phase Stabilization of α-$CsPbI_3$ Perovskite for High-Efficiency Photovoltaics. *Science* **2016**, *354*, 92−95.
(100) Sharma, S.; Weiden, N.; Weiss, A. Phase-Diagrams of Quasi-Binary Systems of the Type - ABX_3-$A'BX_3$ ABX_3-$AB'X_3$, and ABX_3-$AB'X'_3$ X = Halogen. *Z. Phys. Chem.* **1992**, *175*, 63−80.
(101) Trots, D. M.; Myagkota, S. V. High-Temperature Structural Evolution of Caesium and Rubidium Triiodoplumbates. *J. Phys. Chem. Solids* **2008**, *69*, 2520−2526.
(102) Stoumpos, C. C.; Malliakas, C. D.; Kanatzidis, M. G. Semiconducting Tin and Lead Iodide Perovskites with Organic Cations: Phase Transitions, High Mobilities, and Near-Infrared Photoluminescent Properties. *Inorg. Chem.* **2013**, *52*, 9019−9038.
(103) Babin, V.; Fabeni, P.; Nikl, M.; Nitsch, K.; Pazzi, G. P.; Zazubovich, S. Luminescent $CsPbI_3$ and Cs_4PbI_6 Aggregates in Annealed CsI: Pb Crystals. *Phys. Status Solidi B* **2001**, *226*, 419−428.
(104) Luo, P.; Xia, W.; Zhou, S.; Sun, L.; Cheng, J.; Xu, C.; Lu, Y. Solvent Engineering for Ambient-Air-Processed, Phase-Stable $CsPbI_3$ in Perovskite Solar Cells. *J. Phys. Chem. Lett.* **2016**, *7*, 3603−3608.
(105) Eperon, G. E.; Paterno, G. M.; Sutton, R. J.; Zampetti, A.; Haghighirad, A. A.; Cacialli, F.; Snaith, H. J. Inorganic Caesium Lead Iodide Perovskite Solar Cells. *J. Mater. Chem. A* **2015**, *3*, 19688−19695.
(106) Juarez-Perez, E. J.; Hawash, Z.; Raga, S. R.; Ono, L. K.; Qi, Y. Thermal Degradation of $CH_3NH_3PbI_3$ Perovskite into NH_3 and CH_3I Gases Observed by Coupled Thermogravimetry-Mass Spectrometry Analysis. *Energy Environ. Sci.* **2016**, *9*, 3406−3410.
(107) Conings, B.; Drijkoningen, J.; Gauquelin, N.; Babayigit, A.; D'Haen, J.; D'Olieslaeger, L.; Ethirajan, A.; Verbeeck, J.; Manca, J.; Mosconi, E.; Angelis, F. D.; Boyen, H.-G. Intrinsic Thermal Instability of Methylammonium Lead Trihalide Perovskite. *Adv. Energy Mater.* **2015**, *5*, 1500477.
(108) Saparov, B.; Mitzi, D. B. Organic−Inorganic Perovskites: Structural Versatility for Functional Materials Design. *Chem. Rev.* **2016**, *116*, 4558−4596.
(109) Han, Q.; Bae, S. H.; Sun, P.; Hsieh, Y. T.; Yang, Y. M.; Rim, Y. S.; Zhao, H.; Chen, Q.; Shi, W.; Li, G. Single Crystal Formamidinium Lead Iodide ($FAPbI_3$): Insight into the Structural, Optical, and Electrical Properties. *Adv. Mater.* **2016**, *28*, 2253−2258.
(110) Saidaminov, M. I.; Abdelhady, A. L.; Maculan, G.; Bakr, O. M. Retrograde Solubility of Formamidinium and Methylammonium Lead Halide Perovskites Enabling Rapid Single Crystal Growth. *Chem. Commun.* **2015**, *51*, 17658−17661.
(111) Liu, Y.; Sun, J.; Yang, Z.; Yang, D.; Ren, X.; Xu, H.; Yang, Z.; Liu, S. 20-mm-Large Single-Crystalline Formamidinium-Perovskite Wafer for Mass Production of Integrated Photodetectors. *Adv. Opt. Mater.* **2016**, *4*, 1829−1837.
(112) Fang, H.-H.; Wang, F.; Adjokatse, S.; Zhao, N.; Loi, M. A. Photoluminescence Enhancement in Formamidinium Lead Iodide Thin Films. *Adv. Funct. Mater.* **2016**, *26*, 4653−4659.
(113) Ma, F.; Li, J.; Li, W.; Lin, N.; Wang, L.; Qiao, J. Stable α/δ Phase Junction of Formamidinium Lead Iodide Perovskites for Enhanced Near-Infrared Emission. *Chem. Sci.* **2016**, *8*, 800.
(114) Travis, W.; Glover, E. N. K.; Bronstein, H.; Scanlon, D. O.; Palgrave, R. G. On the Application of the Tolerance Factor to Inorganic and Hybrid Halide Perovskites: a Revised System. *Chem. Sci.* **2016**, *7*, 4548−4556.
(115) Goldschmidt, V. M. Die Gesetze der Krystallochemie. *Naturwissenschaften* **1926**, *14*, 477−485.
(116) Kieslich, G.; Sun, S.; Cheetham, A. K. An Extended Tolerance Factor Approach for Organic−Inorganic Perovskites. *Chem. Sci.* **2015**, *6*, 3430−3433.
(117) Kieslich, G.; Sun, S.; Cheetham, A. K. Solid-State Principles Applied to Organic−Inorganic Perovskites: New Tricks for an Old Dog. *Chem. Sci.* **2014**, *5*, 4712−4715.
(118) Filip, M. R.; Eperon, G. E.; Snaith, H. J.; Giustino, F. Steric Engineering of Metal-Halide Perovskites with Tunable Optical Band Gaps. *Nat. Commun.* **2014**, *5*, 5757.
(119) Li, Z.; Yang, M.; Park, J.-S.; Wei, S.-H.; Berry, J. J.; Zhu, K. Stabilizing Perovskite Structures by Tuning Tolerance Factor: Formation of Formamidinium and Cesium Lead Iodide Solid-State Alloys. *Chem. Mater.* **2016**, *28*, 284−292.
(120) Mitzi, D. B.; Feild, C. A.; Schlesinger, Z.; Laibowitz, R. B. Transport, Optical, and Magnetic-Properties of the Conducting Halide Perovskite $CH_3NH_3SnI_3$. *J. Solid State Chem.* **1995**, *114*, 159−163.
(121) Yokoyama, T.; Cao, D. H.; Stoumpos, C. C.; Song, T.-B.; Sato, Y.; Aramaki, S.; Kanatzidis, M. G. Overcoming Short-Circuit in Lead-Free CH_3NH_3SnI3 Perovskite Solar Cells *via* Kinetically Controlled Gas−Solid Reaction Film Fabrication Process. *J. Phys. Chem. Lett.* **2016**, *7*, 776−782.
(122) Koh, T. M.; Krishnamoorthy, T.; Yantara, N.; Shi, C.; Leong, W. L.; Boix, P. P.; Grimsdale, A. C.; Mhaisalkar, S. G.; Mathews, N. Formamidinium Tin-Based Perovskite with Low Eg for Photovoltaic Applications. *J. Mater. Chem. A* **2015**, *3*, 14996−15000.
(123) Lee, S. J.; Shin, S. S.; Kim, Y. C.; Kim, D.; Ahn, T. K.; Noh, J. H.; Seo, J.; Seok, S. I. Fabrication of Efficient Formamidinium Tin Iodide Perovskite Solar Cells through SnF_2−Pyrazine Complex. *J. Am. Chem. Soc.* **2016**, *138*, 3974−3977.
(124) Wang, J.; Peng, J.; Sun, Y.; Liu, X.; Chen, Y.; Liang, Z. $FAPbCl_3$ Perovskite as Alternative Interfacial Layer for Highly Efficient and Stable Polymer Solar Cells. *Adv. Electron. Mater.* **2016**, *2*, 1600329.
(125) Jang, D. M.; Kim, D. H.; Park, K.; Park, J.; Lee, J. W.; Song, J. K. Ultrasound Synthesis of Lead Halide Perovskite Nanocrystals. *J. Mater. Chem. C* **2016**, *4*, 10625−10629.
(126) Butler, K. T.; Svane, K.; Kieslich, G.; Cheetham, A. K.; Walsh, A. Microscopic Origin of Entropy-Driven Polymorphism in Hybrid Organic-Inorganic Perovskite Materials. *Phys. Rev. B: Condens. Matter Mater. Phys.* **2016**, *94*, 180103.
(127) Chen, T.; Foley, B. J.; Park, C.; Brown, C. M.; Harriger, L. W.; Lee, J.; Ruff, J.; Yoon, M.; Choi, J. J.; Lee, S.-H. Entropy-Driven Structural Transition and Kinetic Trapping in Formamidinium Lead

DOI: 10.1021/acsnano.7b00116
ACS Nano 2017, 11, 3119−3134

Iodide Perovskite. *Science Adv.* **2016**, *2*, e160165010.1126/sciadv.1601650.
(128) Amat, A.; Mosconi, E.; Ronca, E.; Quarti, C.; Umari, P.; Nazeeruddin, M. K.; Grätzel, M.; De Angelis, F. Cation-Induced Band-Gap Tuning in Organohalide Perovskites: Interplay of Spin−Orbit Coupling and Octahedra Tilting. *Nano Lett.* **2014**, *14*, 3608−3616.
(129) Fabini, D. H.; Stoumpos, C. C.; Laurita, G.; Kaltzoglou, A.; Kontos, A. G.; Falaras, P.; Kanatzidis, M. G.; Seshadri, R. Reentrant Structural and Optical Properties and Large Positive Thermal Expansion in Perovskite Formamidinium Lead Iodide. *Angew. Chem., Int. Ed.* **2016**, *55*, 15392−15396.
(130) Sato, T.; Takagi, S.; Deledda, S.; Hauback, B. C.; Orimo, S.-I. Extending the Applicability of the Goldschmidt Tolerance Factor to Arbitrary Ionic Compounds. *Sci. Rep.* **2016**, *6*, 23592.
(131) Hanusch, F. C.; Wiesenmayer, E.; Mankel, E.; Binek, A.; Angloher, P.; Fraunhofer, C.; Giesbrecht, N.; Feckl, J. M.; Jaegermann, W.; Johrendt, D.; Bein, T.; Docampo, P. Efficient Planar Heterojunction Perovskite Solar Cells Based on Formamidinium Lead Bromide. *J. Phys. Chem. Lett.* **2014**, *5*, 2791−2795.
(132) Mashiyama, H.; Kurihara, Y.; Azetsu, T. Disordered Cubic Perovskite Structure of $CH_3NH_3PbX_3$ (X= Cl, Br, I). *J. Korean Phys. Soc.* **1998**, *32*, S156−S158.
(133) Poglitsch, A.; Weber, D. Dynamic Disorder in Methylammoniumtrihalogenoplumbates (II) Observed by Millimeter-Wave Spectroscopy. *J. Chem. Phys.* **1987**, *87*, 6373−6378.
(134) Glazer, A. The Classification of Tilted Octahedra in Perovskites. *Acta Crystallogr., Sect. B: Struct. Crystallogr. Cryst. Chem.* **1972**, *28*, 3384−3392.
(135) Sutton, R. J.; Eperon, G. E.; Miranda, L.; Parrott, E. S.; Kamino, B. A.; Patel, J. B.; Horantner, M. T.; Johnston, M. B.; Haghighirad, A. A.; Moore, D. T.; Snaith, H. J. Bandgap-Tunable Cesium Lead Halide Perovskites with High Thermal Stability for Efficient Solar Cells. *Adv. Energy Mater.* **2016**, *6*, 1502458.
(136) Beal, R. E.; Slotcavage, D. J.; Leijtens, T.; Bowring, A. R.; Belisle, R. A.; Nguyen, W. H.; Burkhard, G. F.; Hoke, E. T.; McGehee, M. D. Cesium Lead Halide Perovskites with Improved Stability for Tandem Solar Cells. *J. Phys. Chem. Lett.* **2016**, *7*, 746−751.
(137) Eperon, G. E.; Stranks, S. D.; Menelaou, C.; Johnston, M. B.; Herz, L. M.; Snaith, H. J. Formamidinium Lead Trihalide: a Broadly Tunable Perovskite for Efficient Planar Heterojunction Solar Cells. *Energy Environ. Sci.* **2014**, *7*, 982−988.
(138) Rehman, W.; Milot, R. L.; Eperon, G. E.; Wehrenfennig, C.; Boland, J. L.; Snaith, H. J.; Johnston, M. B.; Herz, L. M. Charge-Carrier Dynamics and Mobilities in Formamidinium Lead Mixed-Halide Perovskites. *Adv. Mater.* **2015**, *27*, 7938−7944.
(139) Yi, C.; Luo, J.; Meloni, S.; Boziki, A.; Ashari-Astani, N.; Gratzel, C.; Zakeeruddin, S. M.; Rothlisberger, U.; Gratzel, M. Entropic Stabilization of Mixed A-Cation ABX_3 Metal Halide Perovskites for High Performance Perovskite Solar Cells. *Energy Environ. Sci.* **2016**, *9*, 656−662.
(140) Yu, Y.; Wang, C.; Grice, C. R.; Shrestha, N.; Chen, J.; Zhao, D.; Liao, W.; Cimaroli, A. J.; Roland, P. J.; Ellingson, R. J.; Yan, Y. Improving the Performance of Formamidinium and Cesium Lead Triiodide Perovskite Solar Cells using Lead Thiocyanate Additives. *ChemSusChem* **2016**, *9*, 3288.
(141) Weber, O. J.; Charles, B.; Weller, M. T. Phase Behaviour and Composition in the Formamidinium-Methylammonium Hybrid Lead Iodide Perovskite Solid Solution. *J. Mater. Chem. A* **2016**, *4*, 15375−15382.
(142) Lee, J.-W.; Kim, D.-H.; Kim, H.-S.; Seo, S.-W.; Cho, S. M.; Park, N.-G. Formamidinium and Cesium Hybridization for Photo- and Moisture-Stable Perovskite Solar Cell. *Adv. Energy Mater.* **2015**, *5*, 1501310.
(143) McMeekin, D. P.; Sadoughi, G.; Rehman, W.; Eperon, G. E.; Saliba, M.; Hörantner, M. T.; Haghighirad, A.; Sakai, N.; Korte, L.; Rech, B.; Johnston, M. B.; Herz, L. M.; Snaith, H. J. A Mixed-Cation Lead Mixed-Halide Perovskite Absorber for Tandem Solar Cells. *Science* **2016**, *351*, 151−155.
(144) Jeon, N. J.; Noh, J. H.; Yang, W. S.; Kim, Y. C.; Ryu, S.; Seo, J.; Seok, S. I. Compositional Engineering of Perovskite Materials for High-Performance Solar Cells. *Nature* **2015**, *517*, 476−480.
(145) Gao, Y.; Peng, X. Crystal Structure Control of CdSe Nanocrystals in Growth and Nucleation: Dominating Effects of Surface *versus* Interior Structure. *J. Am. Chem. Soc.* **2014**, *136*, 6724−6732.
(146) Yu, W. W.; Wang, Y. A.; Peng, X. Formation and Stability of Size-, Shape-, and Structure-Controlled CdTe Nanocrystals: Ligand Effects on Monomers and Nanocrystals. *Chem. Mater.* **2003**, *15*, 4300−4308.
(147) Fu, Y.; Zhu, H.; Schrader, A. W.; Liang, D.; Ding, Q.; Joshi, P.; Hwang, L.; Zhu, X. Y.; Jin, S. Nanowire Lasers of Formamidinium Lead Halide Perovskites and Their Stabilized Alloys with Improved Stability. *Nano Lett.* **2016**, *16*, 1000−1008.
(148) Protesescu, L.; Yakunin, S.; Bodnarchuk, M. I.; Bertolotti, F.; Masciocchi, N.; Guagliardi, A.; Kovalenko, M. V. Monodisperse Formamidinium Lead Bromide Nanocrystals with Bright and Stable Green Photoluminescence. *J. Am. Chem. Soc.* **2016**, *138*, 14202−14205.
(149) Weidman, M. C.; Seitz, M.; Stranks, S. D.; Tisdale, W. A. Highly Tunable Colloidal Perovskite Nanoplatelets through Variable Cation, Metal, and Halide Composition. *ACS Nano* **2016**, *10*, 7830−7839.
(150) Tsai, H.; Nie, W.; Blancon, J.-C.; Stoumpos, C. C.; Asadpour, R.; Harutyunyan, B.; Neukirch, A. J.; Verduzco, R.; Crochet, J. J.; Tretiak, S.; Pedesseau, L.; Even, J.; Alam, M. A.; Gupta, G.; Lou, J.; Ajayan, P. M.; Bedzyk, M. J.; Kanatzidis, M. G.; Mohite, A. D. High-Efficiency Two-Dimensional Ruddlesden−Popper Perovskite Solar Cells. *Nature* **2016**, *536*, 312−316.
(151) Willmott, P. R.; Meister, D.; Leake, S. J.; Lange, M.; Bergamaschi, A.; Boge, M.; Calvi, M.; Cancellieri, C.; Casati, N.; Cervellino, A.; Chen, Q.; David, C.; Flechsig, U.; Gozzo, F.; Henrich, B.; Jaggi-Spielmann, S.; Jakob, B.; Kalichava, I.; Karvinen, P.; Krempasky, J.; et al. The Materials Science Beamline Upgrade at the Swiss Light Source. *J. Synchrotron Radiat.* **2013**, *20*, 667−682.
(152) Weller, M. T.; Weber, O. J.; Frost, J. M.; Walsh, A. Cubic Perovskite Structure of Black Formamidinium Lead Iodide, α-$[HC(NH_2)_2]PbI_3$, at 298 K. *J. Phys. Chem. Lett.* **2015**, *6*, 3209−3212.
(153) Sakata, M.; Harada, J.; Cooper, M. J.; Rouse, K. D. Neutron-Diffraction Study of Anharmonic Thermal Vibrations in Cubic $CsPbX_3$. *Acta Crystallogr., Sect. A: Cryst. Phys., Diffr., Theor. Gen. Crystallogr.* **1980**, *36*, 7−15.
(154) Cervellino, A.; Frison, R.; Bertolotti, F.; Guagliardi, A. DEBUSSY 2.0: TheNew Release of a Debye User System for Nanocrystalline and/or Disordered Materials. *J. Appl. Crystallogr.* **2015**, *48*, 2026−2032.
(155) Debye, P. X-ray Dispersal. *Ann. Phys.* **1915**, *46*, 809−823.
(156) Zhou, Z.; Pang, S.; Ji, F.; Zhang, B.; Cui, G. The Fabrication of Formamidinium Lead Iodide Perovskite Thin Films *via* Organic Cation Exchange. *Chem. Commun.* **2016**, *52*, 3828−3831.
(157) Eperon, G. E.; Beck, C. E.; Snaith, H. J. Cation Exchange for Thin Film Lead Iodide Perovskite Interconversion. *Mater. Horiz.* **2016**, *3*, 63−71.
(158) Zhou, Y.; Yang, M.; Pang, S.; Zhu, K.; Padture, N. P. Exceptional Morphology-Preserving Evolution of Formamidinium Lead Triiodide Perovskite Thin Films *via* Organic-Cation Displacement. *J. Am. Chem. Soc.* **2016**, *138*, 5535−5538.
(159) Bourdakos, K. N.; Dissanayake, D.; Lutz, T.; Silva, S. R. P.; Curry, R. J. Highly Efficient Near-Infrared Hybrid Organic-Inorganic Nanocrystal Electroluminescence Device. *Appl. Phys. Lett.* **2008**, *92*, 153311.
(160) Gong, X.; Yang, Z.; Walters, G.; Comin, R.; Ning, Z.; Beauregard, E.; Adinolfi, V.; Voznyy, O.; Sargent, E. H. Highly Efficient Quantum Dot Near-Infrared Light-Emitting Diodes. *Nat. Photonics* **2016**, *10*, 253−257.
(161) Aharon, S.; Dymshits, A.; Rotem, A.; Etgar, L. Temperature Dependence of Hole Conductor Free Formamidinium Lead Iodide Perovskite Based Solar Cells. *J. Mater. Chem. A* **2015**, *3*, 9171−9178.

DOI: 10.1021/acsnano.7b00116
ACS Nano 2017, 11, 3119−3134

(162) Qin, L.; Lv, L.; Ning, Y.; Li, C.; Lu, Q.; Zhu, L.; Hu, Y.; Lou, Z.; Teng, F.; Hou, Y. Enhanced Amplified Spontaneous Emission from Morphology-Controlled Organic-Inorganic Halide Perovskite Films. *RSC Adv.* **2015**, *5*, 103674−103679.
(163) Stranks, S. D.; Wood, S. M.; Wojciechowski, K.; Deschler, F.; Saliba, M.; Khandelwal, H.; Patel, J. B.; Elston, S. J.; Herz, L. M.; Johnston, M. B.; Schenning, A. P. H. J.; Debije, M. G.; Riede, M. K.; Morris, S. M.; Snaith, H. J. Enhanced Amplified Spontaneous Emission in Perovskites Using a Flexible Cholesteric Liquid Crystal Reflector. *Nano Lett.* **2015**, *15*, 4935−4941.
(164) Wang, Y.; Li, X.; Song, J.; Xiao, L.; Zeng, H.; Sun, H. All-Inorganic Colloidal Perovskite Quantum Dots: A New Class of Lasing Materials with Favorable Characteristics. *Adv. Mater.* **2015**, *27*, 7101−7108.
(165) Eaton, S. W.; Lai, M.; Gibson, N. A.; Wong, A. B.; Dou, L.; Ma, J.; Wang, L.-W.; Leone, S. R.; Yang, P. Lasing in Robust Cesium Lead Halide Perovskite Nanowires. *Proc. Natl. Acad. Sci. U. S. A.* **2016**, *113*, 1993−1998.
(166) She, C.; Fedin, I.; Dolzhnikov, D. S.; Dahlberg, P. D.; Engel, G. S.; Schaller, R. D.; Talapin, D. V. Red, Yellow, Green, and Blue Amplified Spontaneous Emission and Lasing Using Colloidal CdSe Nanoplatelets. *ACS Nano* **2015**, *9*, 9475−9485.
(167) She, C.; Fedin, I.; Dolzhnikov, D. S.; Demortière, A.; Schaller, R. D.; Pelton, M.; Talapin, D. V. Low-Threshold Stimulated Emission Using Colloidal Quantum Wells. *Nano Lett.* **2014**, *14*, 2772−2777.
(168) Veldhuis, S. A.; Boix, P. P.; Yantara, N.; Li, M.; Sum, T. C.; Mathews, N.; Mhaisalkar, S. G. Perovskite Materials for Light-Emitting Diodes and Lasers. *Adv. Mater.* **2016**, *28*, 6804−6834.
(169) Xing, G.; Kumar, M. H.; Chong, W. K.; Liu, X.; Cai, Y.; Ding, H.; Asta, M.; Grätzel, M.; Mhaisalkar, S.; Mathews, N.; Sum, T. C. Solution-Processed Tin-Based Perovskite for Near-Infrared Lasing. *Adv. Mater.* **2016**, *28*, 8191−8196.
(170) Grabolle, M.; Spieles, M.; Lesnyak, V.; Gaponik, N.; Eychmüller, A.; Resch-Genger, U. Determination of the Fluorescence Quantum Yield of Quantum Dots: Suitable Procedures and Achievable Uncertainties. *Anal. Chem.* **2009**, *81*, 6285−6294.
(171) Rurack, K.; Spieles, M. Fluorescence Quantum Yields of a Series of Red and Near-Infrared Dyes Emitting at 600−1000 nm. *Anal. Chem.* **2011**, *83*, 1232−1242.
(172) Semonin, O. E.; Johnson, J. C.; Luther, J. M.; Midgett, A. G.; Nozik, A. J.; Beard, M. C. Absolute Photoluminescence Quantum Yields of IR-26 Dye, PbS, and PbSe Quantum Dots. *J. Phys. Chem. Lett.* **2010**, *1*, 2445−2450.
(173) Bergamaschi, A.; Cervellino, A.; Dinapoli, R.; Gozzo, F.; Henrich, B.; Johnson, I.; Kraft, P.; Mozzanica, A.; Schmitt, B.; Shi, X. T. The MYTHEN Detector for X-Ray Powder Diffraction Experiments at the Swiss Light Source. *J. Synchrotron Radiat.* **2010**, *17*, 653−668.
(174) Doolittle, L. R. A Semiautomatic Algorithm for Rutherford Backscattering Analysis. *Nucl. Instrum. Methods Phys. Res., Sect. B* **1986**, *15*, 227−231.

DOI: 10.1021/acsnano.7b00116
ACS Nano 2017, 11, 3119−3134